

The second Sandia Fracture Challenge: blind prediction of dynamic shear localization and full fracture characterization

Keunhwan Pack · Christian C. Roth

Received: 10 August 2015 / Accepted: 9 February 2016 / Published online: 22 February 2016
© Springer Science+Business Media Dordrecht 2016

Abstract In the context of the second Sandia Fracture Challenge, dynamic tensile experiments performed on a Ti–6Al–4V alloy with a complex fracture specimen geometry are modeled numerically. Sandia National Laboratories provided the participants with limited experimental data, comprising of uniaxial tensile test and V-notched rail shear test results. To model the material behavior up to large plastic strains, the flow stress is described with a linear combination of Swift and Voce strain hardening laws in conjunction with the inverse method. The effect of the strain rate and temperature is incorporated through the Johnson–Cook strain rate hardening and temperature softening functions. A strain rate dependent weighting function is used to compute the fraction of incremental plastic work converted to heat. The Hill’48 anisotropic yield function is adopted to capture weak deformation resistance under in-plane pure shear stress. Fracture initiation is predicted by the recently developed strain rate dependent Hosford–Coulomb fracture criterion. The calibration procedure is described in detail, and a good agreement between the blind prediction and the experiments at two

different speeds is obtained for both the crack path and the force–crack opening displacement (COD) curve. A comprehensive experimental and numerical follow-up study on leftover material is conducted, and plasticity and fracture parameters are carefully re-calibrated. A more elaborate modeling approach using a non-associated flow rule is pursued, and the fracture locus of the Ti–6Al–4V is clearly identified by means of four different fracture specimens covering a wide range of stress states and strain rates. With the full characterization, a noticeable improvement in the force–COD curve is obtained. In addition, the effect of friction is studied numerically.

Keywords Sandia Fracture Challenge · Ductile fracture · Dynamic · Shear localization · Hosford · Triaxiality · Lode angle · Ti–6Al–4V

1 Introduction

In 2012, Sandia National Laboratories (SNL) announced an intriguing round robin challenge for the fracture mechanics community. Thirteen participating teams were provided with a limited number of elementary test data on a typical stainless steel sheet and asked to make a blind prediction of crack initiation and propagation for a modified compact tension specimen with a round starter notch and three randomly distributed holes subjected to tensile loading (Boyce 2014). A variety of modeling approaches were taken; from porous plastic-

K. Pack (✉) · C. C. Roth
Impact and Crashworthiness Laboratory, Department of
Mechanical Engineering, Massachusetts Institute of
Technology, Cambridge, MA, USA
e-mail: kpack@mit.edu

C. C. Roth
Department of Mechanical and Process Engineering,
ETH Zurich, Zurich, Switzerland
e-mail: ccroth@mit.edu

ity (Cerrone et al. 2014 and Nahshon et al. 2014) to extended finite element methods (Zhang et al. 2014) and damage indicator models uncoupled from plasticity (Gross and Ravi-Chandar 2014; Neilsen et al. 2014; Pack et al. 2014). This was an opportunity for the community to evaluate their current modeling capability and identify missing information essential to improve prediction. After fully characterizing spare material, Pack et al. (2014) pointed out that an accurate description of the hardening behavior at large strains is crucial in capturing localization and subsequent crack development.

The successful completion of the first challenge was followed by the second challenge in 2014 (Boyce et al. 2016), examining the effect of dynamic loading on ductile fracture of a titanium alloy Ti–6Al–4V sheet. Two loading speeds were selected: 0.0254 mm/s for the slow loading case and 25.4 mm/s for the fast loading case. Besides data from basic uniaxial tensile tests on dog-bone shaped specimens (engineering stress–strain curves at the two loading speeds), only results of V-notched rail shear tests (force–displacement curves at the two loading speeds) were additionally provided. The shear test was suggested by former participants to further characterize the material behavior under shear dominant loading. The geometry of the challenge specimen was S-shaped with two circular notches and three different-sized holes. The participants were asked to report their numerical prediction of crack paths as well as force–crack opening displacement (COD) curves. Answers were allowed to include upper and lower boundaries.

Ductile fracture of metallic materials is one of the most common failure modes, ranging from the integrity of a large structure such as buildings, bridges, and off-shore installations to the safety of automobiles, ships, and aircrafts. Ductile fracture on a microscopic scale is understood as a consequence of void nucleation, growth, and coalescence. Various approaches have been taken to model this phenomenon. The theory of porous plasticity, introduced by Gurson (1977), mathematically formulates the aforementioned micro-mechanism by incorporating the effect of a current void volume fraction on the macroscopic plastic flow. Fracture is said to occur when the void volume fraction reaches a critical value. The original model was enriched by Tvergaard and Needleman (1984) and Nahshon and Hutchinson (2008). The latter modification was particularly aimed at accumulating damage

due to void shearing, which was also considered by Xue (2008). Another avenue for modeling ductile fracture was introduced by Lemaitre (1985) who used the idea of an effective stress carried by an effective area of a damaged material and derived that the elastic properties are altered accordingly. The other group of modeling methods uses a damage indicator concept. Herein, elastic and plastic properties remain unaffected, and fracture is said to occur once a damage indicator reaches a critical value. Typical examples include McClintock (1968), Rice and Tracey (1969), Bai and Wierzbicki (2010), and Lou et al. (2012). Recently, Roth and Mohr (2014) developed a strain rate dependent Hosford–Coulomb fracture initiation model, which was initially proposed by Mohr and Marcadet (2015) in a strain rate independent form.

Furthermore, the innate anisotropy of thin structures, due to the manufacturing process (e.g. rolling), has also been a research topic of interest to the metal forming community. To address this effect, Hill (1948) suggested a quadratic anisotropic yield function for orthotropic materials, while Barlat et al. (2003) introduced a linear transformation to the well-known Hosford (1972) plasticity for aluminum sheets. To capture the pronounced anisotropy in yield stresses and plastic strain ratios, Stoughton (2002) proposed a non-associated flow rule with two quadratic potentials. Furthermore, Huh et al. (2013) showed that the plane anisotropy of advanced high strength steel sheets exhibits strain rate dependence.

A wide variety of models for dynamic loading have been studied extensively in the literature. They can be divided into physics-based models (Kocks et al. 1975; Zerilli and Armstrong 1987; Khan and Huang 1992; Rusinek and Klepaczko 2001; Voyiadjis and Abed 2005), which are usually inspired by thermodynamics and dislocation dynamics, and phenomenological/empirical models. One of the most popular phenomenological models is based on the work by Johnson and Cook (1983). Herein a multiplicative decomposition of the flow stresses from a strain, strain rate, and temperature term is postulated. It has been shown in several pieces of work that it provides a reasonable prediction of temperature-dependent viscoplastic response up to large strains (e.g. Clausen et al. 2004; Smerd et al. 2005; Verleysen et al. 2011; Erice et al. 2012). Recently, Roth and Mohr (2014) coupled the Johnson–Cook plasticity model with a combined Swift–Voce strain hardening function and a non-associated anisotropic flow rule,

obtaining very good results for two different advanced high strength steels.

The present paper describes in detail the modeling efforts made by the Impact and Crashworthiness Laboratory (ICL) at Massachusetts Institute of Technology (MIT) for the second Sandia Fracture Challenge. In the following section, the plasticity and fracture models chosen to model the titanium alloy are briefly reviewed. Next, the calibration procedures based on the limited number of test data provided by SNL are comprehensively presented. The sequence of deformation predicted by blind simulation is thoroughly analyzed and compared with the experimental results that were disclosed to the participants after the blind prediction. In the fourth section, a full characterization of the Ti–6Al–4V alloy is performed. It comprises of an extensive testing program at slow and fast loading speeds, including uniaxial tensile tests in three in-plane directions and four types of fracture experiments, and the recalibration of the plasticity and fracture models. Finally, the simulation results of the challenge specimen geometry based on the more advanced calibration of the material models are evaluated and discussed.

2 Rate-dependent plasticity and fracture model

This section is devoted to presenting the constitutive law and the fracture model that were used to describe the plasticity and fracture response of the Ti–6Al–4V sheet.

2.1 Material

The material chosen for the challenge is a 3.124 mm thick mill-annealed sheet of a Ti–6Al–4V alloy, the most commonly used titanium alloy due to its significantly improved strength over a pure metal state. Its chemical composition is given in Table 1. It is an

Table 1 Alloying elements of the Ti–6Al–4V alloy sheet (all in wt%)

Al	V	C	Fe	O	N	Y
6.02	3.94	0.01	0.19	0.16	0.04	< 50 ppm

alpha plus beta alloy, meaning that the hexagonal close-packed phase and the body-centered cubic phase co-exist. The alloy is known to exhibit a high yield stress, a relatively low strain hardening, and a moderate strain rate sensitivity. Its wide applications cover airframes, vessels, fasteners, blades, and forgings. Notable properties include its excellent biocompatibility.

2.2 Rate-dependent plasticity model

The plastic behavior of the Ti–6Al–4V sheet is described by a conventional theory of metal plasticity in continuum mechanics, namely a yield function, a flow rule, and a hardening law, closely following [Roth and Mohr \(2014\)](#). The following subsections briefly explain a specific model used for each constituent.

2.2.1 Yield function

The simple yet effective Hill’48 quadratic yield function ([Hill 1948](#)) is chosen to account for the in-plane anisotropy of the sheet. Hereinafter, we make use of the notation proposed by [Mohr et al. \(2010\)](#).

$$f = \bar{\sigma}_{Hill} - k = \sqrt{(\mathbf{P}\boldsymbol{\sigma}) \cdot \boldsymbol{\sigma}} - k \tag{1}$$

The Mandel–Voigt notation is used to represent the symmetric Cauchy stress $\boldsymbol{\sigma}$, while k denotes the deformation resistance that defines the boundary of an elastic set. \mathbf{P} describes the positive definite 6×6 matrix in the case of a general three-dimensional stress state.

$$\mathbf{P} = \begin{bmatrix} 1 & P_{12} & -(1 + P_{12}) & 0 & 0 & 0 \\ P_{12} & P_{22} & -(P_{12} + P_{22}) & 0 & 0 & 0 \\ -(1 + P_{12}) & -(P_{12} + P_{22}) & 1 + 2P_{12} + P_{22} & 0 & 0 & 0 \\ 0 & 0 & 0 & P_{44} & 0 & 0 \\ 0 & 0 & 0 & 0 & 3 & 0 \\ 0 & 0 & 0 & 0 & 0 & 3 \end{bmatrix} \tag{2}$$

The expanded form for Eq. (1) reads as

$$\bar{\sigma}_{Hill} = \sqrt{\sigma_{11}^2 + P_{22}\sigma_{22}^2 + (1 + 2P_{12} + P_{22})\sigma_{33}^2 + 2P_{12}\sigma_{11}\sigma_{22} - 2(P_{12} + P_{22})\sigma_{22}\sigma_{33} - 2(1 + P_{12})\sigma_{33}\sigma_{11} + P_{44}\sigma_{12}^2 + 3\sigma_{23}^2 + 3\sigma_{31}^2}. \tag{3}$$

The yield stress ratios for uniaxial tension in three typical directions i.e. rolling, diagonal, and transverse directions (RD, DD, and TD, respectively) and for equibiaxial tension or pure shear determine three independent parameters, P_{12} , P_{22} and P_{44} . For the special case of $P_{12} = -0.5$, $P_{22} = 1$ and $P_{44} = 3$, the well-known von-Mises J2 isotropic yield function is obtained.

2.2.2 Flow rule

To incorporate the effect of a different directionality of the r-values from the yield stresses without losing advantages of quadratic functions, [Stoughton \(2002\)](#) introduced a potential function g in addition to the yield function f and assumed that the direction of the plastic flow is aligned with the stress derivative of the plastic flow potential g . Thus, a non-associated flow rule is obtained.

$$d\mathbf{\epsilon}_p = d\lambda \frac{\partial g[\boldsymbol{\sigma}]}{\partial \boldsymbol{\sigma}} \text{ with } d\mathbf{\epsilon}_p = [d\epsilon_{11}^p \ d\epsilon_{22}^p \ d\epsilon_{33}^p \ d\gamma_{12}^p \ d\gamma_{23}^p \ d\gamma_{31}^p]^T \tag{4}$$

$d\gamma_{ij}^p$ denotes the plastic engineering shear strain. Based on the notation proposed by [Mohr et al. \(2010\)](#), the plastic flow potential is written as

$$g = \sqrt{(\mathbf{G}\boldsymbol{\sigma}) \cdot \boldsymbol{\sigma}}. \tag{5}$$

\mathbf{G} can be obtained by replacing P_{ij} in Eq. (2) with G_{ij} . It is noted that the non-associated flow rule reduces to an associated one for $G_{12} = P_{12}$, $G_{22} = P_{22}$, and $G_{44} = P_{44}$.

The equivalent plastic strain increment $d\bar{\epsilon}_p$ is defined as work-conjugate to the equivalent stress through the identity

$$\boldsymbol{\sigma} \cdot d\mathbf{\epsilon}_p = \bar{\sigma}_{Hill} d\bar{\epsilon}_p. \tag{6}$$

2.2.3 Hardening law

The isotropic hardening function k in Eq. (1) governs the growth of the radius of the yield surface. With dynamic loading conditions being considered in the

second Sandia Fracture Challenge, the model proposed by [Roth and Mohr \(2014\)](#) is employed. The deformation resistance k uses the equivalent plastic strain $\bar{\epsilon}_p$, the equivalent plastic strain rate $\dot{\bar{\epsilon}}_p$, and temperature T as internal variables. Inspired by the work by [Johnson and Cook \(1983\)](#), the model suggests the multiplicative decomposition of the three effects:

$$k[\bar{\epsilon}_p, \dot{\bar{\epsilon}}_p, T] = k_\epsilon[\bar{\epsilon}_p] k_{\dot{\epsilon}}[\dot{\bar{\epsilon}}_p] k_T[T]. \tag{7}$$

The strain hardening function k_ϵ reads as

$$k_\epsilon[\bar{\epsilon}_p] = \alpha A (\bar{\epsilon}_p + \epsilon_0)^n + (1 - \alpha) \left(k_0 + Q \left(1 - e^{-\beta \bar{\epsilon}_p} \right) \right). \tag{8}$$

It is a linear combination of a power law ([Swift 1952](#)) and an exponential law ([Voce 1948](#)) using the weighting parameter α . Equation (8) proved to be suitable for large strains beyond necking for a wide variety of steels ([Roth and Mohr 2014](#); [Marcadet and Mohr 2015](#); [Pack and Marcadet 2016](#)).

The strain rate hardening function $k_{\dot{\epsilon}}$ and the temperature softening function k_T are in the standard Johnson–Cook form and read as

$$k_{\dot{\epsilon}}[\dot{\bar{\epsilon}}_p] = \begin{cases} 1 & \text{for } \dot{\bar{\epsilon}}_p < \dot{\epsilon}_0 \\ 1 + C \ln \left[\frac{\dot{\bar{\epsilon}}_p}{\dot{\epsilon}_0} \right] & \text{for } \dot{\bar{\epsilon}}_p \geq \dot{\epsilon}_0 \end{cases}, \tag{9}$$

$$k_T[T] = \begin{cases} 1 & \text{for } T < T_r \\ 1 - \left(\frac{T - T_r}{T_m - T_r} \right)^m & \text{for } T_r \leq T \leq T_m \end{cases} \tag{10}$$

with the strain rate sensitivity C , the reference strain rate $\dot{\epsilon}_0$, the temperature softening exponent m , the reference temperature T_r , and the melting temperature T_m . Note that both functions reduce to unity for $\dot{\bar{\epsilon}}_p < \dot{\epsilon}_0$ and $T < T_r$, respectively.

2.3 Temperature evolution

To account for the increase in temperature due to plastic work, a fully coupled thermo-mechanical analysis is normally required, treating the temperature as an external state variable. Even though this is often neglected

because of higher computational costs or uncertainties in the boundary conditions, temperature softening plays an important role in the post-necking behavior of a material. As shown in [Roth and Mohr \(2014\)](#), a purely mechanical analysis is used, treating the temperature as an internal state variable determined from

$$\rho C_p dT = \omega[\dot{\epsilon}_p] \eta_k \bar{\sigma}_{Hill} d\bar{\epsilon}_p. \tag{11}$$

Herein, ρ , C_p , and η_k are density, heat capacity and the Taylor–Quinney coefficient, respectively. The strain rate dependent conversion factor $\omega[\dot{\epsilon}_p]$ varies smoothly from the isothermal condition ($\omega = 0$) with complete heat dissipation to the adiabatic condition ($\omega = 1$) where no time is allowed for dissipation:

$$\omega[\dot{\epsilon}_p] = \begin{cases} 0 & \text{for } \dot{\epsilon}_p < \dot{\epsilon}_{it} \\ \frac{(\dot{\epsilon}_p - \dot{\epsilon}_{it})^2 (3\dot{\epsilon}_a - 2\dot{\epsilon}_p - \dot{\epsilon}_{it})}{(\dot{\epsilon}_a - \dot{\epsilon}_{it})^3} & \text{for } \dot{\epsilon}_{it} \leq \dot{\epsilon}_p \leq \dot{\epsilon}_a \\ 1 & \text{for } \dot{\epsilon}_a < \dot{\epsilon}_p \end{cases} \tag{12}$$

$\dot{\epsilon}_{it}$, greater than zero, indicates the isothermal limit below which no temperature increase takes place, and $\dot{\epsilon}_a$, greater than $\dot{\epsilon}_{it}$, defines the adiabatic limit beyond which the conversion of plastic work into heat is maximized. It is stressed that $\dot{\epsilon}_p$ in the above formulae represents a local strain rate at each material point and is not a function of the global loading speed. For additional information, the reader is referred to [Roth and Mohr \(2014\)](#).

2.4 Rate dependent Hosford–Coulomb fracture initiation model

For the numerical prediction of fracture initiation, the strain rate modified version of the Hosford–Coulomb model ([Roth and Mohr 2014](#)) is used. It is supported by the results of a computational localization analysis of a unit cell by [Dunand and Mohr \(2014\)](#). The Hosford–Coulomb model presents a very similar fracture envelope to the modified Mohr–Coulomb model ([Bai and Wierzbicki 2010](#)), but it is mathematically and physically more consistent with the chosen plasticity model. More specifically, the stress triaxiality and Lode angle dependent hardening law ([Bai and Wierzbicki 2008](#)) does not have to be applied in transforming stress at fracture to strain at fracture.

2.4.1 Characterization of stress states

The fracture mechanics community has long been using the stress triaxiality η as the main scalar variable that characterizes a current stress state. It is defined as the ratio of mean stress σ_m to the von-Mises equivalent stress $\bar{\sigma}_{VM}$.

$$\eta = \frac{\sigma_m}{\bar{\sigma}_{VM}}, \text{ where } \sigma_m = \frac{\sigma_{11} + \sigma_{22} + \sigma_{33}}{3} \text{ and } \bar{\sigma}_{VM} = \sqrt{\frac{3}{2} \boldsymbol{\sigma}' : \boldsymbol{\sigma}'} \tag{13}$$

$\boldsymbol{\sigma}'$ denotes the second-order deviatoric Cauchy stress tensor. This concept reflects a fundamental microscopic mechanism that ductile fracture is a result of void nucleation, growth, and coalescence. However, unusual dependence of strain to fracture on η between simple shear to simple tension observed by [Bao and Wierzbicki \(2004\)](#) inspired [Xue \(2007\)](#) to introduce the second measure of stress state, the Lode angle parameter $\bar{\theta}$, as the other key variable to control ductility.

$$\bar{\theta} = 1 - \frac{6\theta}{\pi} \quad (-1 \leq \bar{\theta} \leq 1) \tag{14}$$

$$\text{where } \theta = \frac{1}{3} \cos^{-1} \left(\frac{27}{2} \frac{J_3}{\bar{\sigma}_{VM}^3} \right) \quad \left(0 \leq \theta \leq \frac{\pi}{3} \right)$$

$$J_3 = \det(\boldsymbol{\sigma}') = \frac{1}{3} \boldsymbol{\sigma}' \cdot \boldsymbol{\sigma}' : \boldsymbol{\sigma}'$$

The two isotropic stress parameters η and $\bar{\theta}$ uniquely determine the direction of a stress vector in the three-dimensional isotropic principal stress space.

2.4.2 Hosford–Coulomb fracture initiation model

[Mohr and Marcadet \(2015\)](#) postulated that an initially un-cracked ductile solid under proportional loading conditions loses its local load bearing capacity, and a macroscopic crack initiates when a critical stress value B is reached by a linear combination of the Hosford equivalent stress and the normal stress on the plane on which the maximum shear stress occurs.

$$\bar{\sigma}_{Hosford} + c(\sigma_I + \sigma_{III}) = B \tag{15}$$

Herein, σ_I and σ_{III} are the maximum and the minimum principal stresses. Through coordinate transformation

one can obtain an expression for $\bar{\epsilon}_f^{pr}$ in the mixed space of stress and strain in the form of Eq. (16):

$$\bar{\epsilon}_f^{pr}[\eta, \bar{\theta}] = b(1 + c)^{\frac{1}{n_f}} \left[\left\{ \frac{1}{2}((f_1 - f_2)^a + (f_2 - f_3)^a + (f_3 - f_1)^a) \right\}^{\frac{1}{a}} + c(2\eta + f_1 + f_3) \right]^{-\frac{1}{n_f}} \tag{16}$$

with

$$\begin{aligned} f_1[\bar{\theta}] &= \frac{2}{3} \cos \left[\frac{\pi}{6} (1 - \bar{\theta}) \right], \\ f_2[\bar{\theta}] &= \frac{2}{3} \cos \left[\frac{\pi}{6} (3 + \bar{\theta}) \right], \\ f_3[\bar{\theta}] &= -\frac{2}{3} \cos \left[\frac{\pi}{6} (1 + \bar{\theta}) \right]. \end{aligned}$$

The main parameters of the model are $\{a, b, c\}$: the Hosford exponent a , controlling the effect of the Lode angle parameter $\bar{\theta}$, the friction coefficient c , controlling the effect of the stress triaxiality η , and the parameter b , a multiplier controlling the overall magnitude of the strain to fracture. The exponent n_f is used to transform the equivalent stress at fracture $\bar{\sigma}_f$ to the equivalent strain $\bar{\epsilon}_f^{pr}$ with a simple power hardening law.

$$\bar{\sigma}_f = A \left(\bar{\epsilon}_f^{pr} \right)^{n_f} \tag{17}$$

This assumption allows for the concise analytical expression of the fracture criterion in Eq. (16) and reduces computational time without the need to perform additional Newton–Raphson iterations with an actual strain hardening law in Eq. (8).

Roth and Mohr (2014) extended the formulation in loose analogy to Johnson and Cook (1983) to incorporate the effect of strain rate on fracture through the parameter b :

$$b = b_0 \left[1 + \gamma \ln \left(\frac{\dot{\epsilon}_p}{\dot{\epsilon}_0} \right) \right] \text{ when } \dot{\epsilon}_p > \dot{\epsilon}_0 \tag{18}$$

The strain to fracture for uniaxial tension at low strain rates is given through $b_0 > 0$, while the strain rate sensitivity of the fracture initiation model is governed by the parameter $\gamma \geq 0$.

Non-proportional loading conditions, for which η and $\bar{\theta}$ vary, are treated by means of a simple linear damage accumulation rule in Eq. (19).

$$D = \int_0^{\bar{\epsilon}_p} \frac{d\bar{\epsilon}_p}{\bar{\epsilon}_f^{pr}[\eta, \bar{\theta}, \dot{\epsilon}_p]} \tag{19}$$

The damage indicator D varies from the initial value $D = 0$ to the maximum value of $D = 1$, for which fracture initiation occurs. It is worth mentioning that Eq. (19) recovers the cumulated equivalent plastic strain to fracture $\bar{\epsilon}_p^f = \bar{\epsilon}_f^{pr}[\eta, \bar{\theta}, \dot{\epsilon}_p]$ for proportional loading paths.

3 Blind simulation of second Sandia Fracture Challenge problem

In this section, the methodology to simulate the second Sandia Fracture Challenge problem based on a very limited number of experimental data is described.

3.1 Model calibration based on SNL experimental results

3.1.1 Plasticity model parameter identification

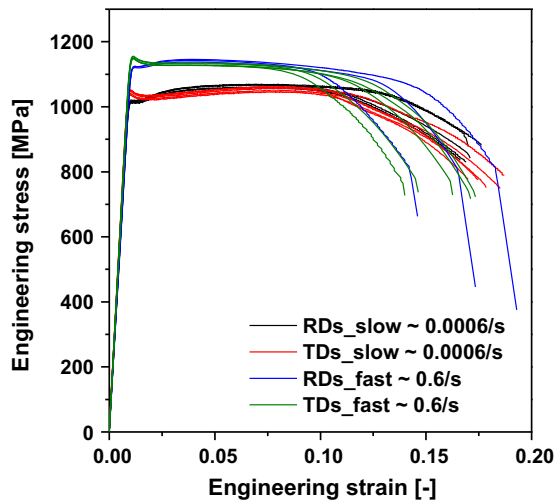
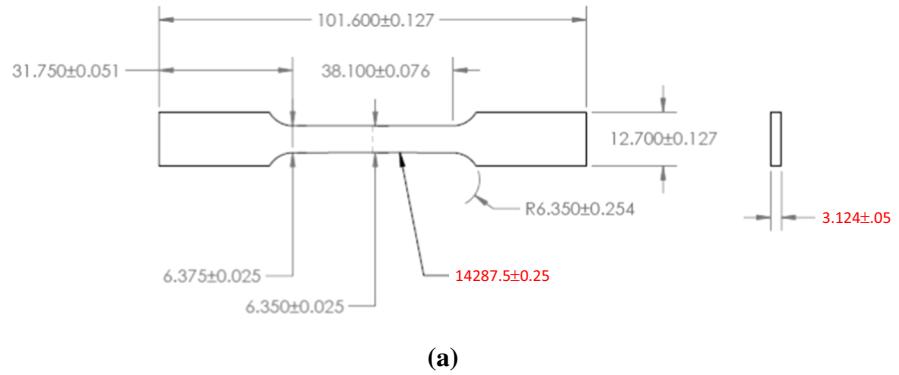
Figure 1b summarizes the results of uniaxial tensile tests on dog-bone shaped specimens (Fig. 1a) cut at 0° and 90° with respect to the sheet rolling direction (RD and TD, respectively). The experiments were performed by SNL at two different loading speeds of 0.0254 and 25.4 mm/s. The nominal strain in the axial direction was measured by a 25.4 mm extensometer, and the corresponding strain rates were about 0.0006 and 0.6/s, respectively. Young’s modulus was calculated to lie in the range of 112 ~ 115 GPa, and the Poisson’s ratio ($\nu = 0.342$) was taken from the MatWeb LLC webpage.

Without the result from the 45° direction (DD) provided to the participants, almost identical hardening curves between the two orthogonal directions suggest a possible isotropy of the material. Hence, initially a von Mises yield surface with $P_{12} = -0.5$, $P_{22} = 1$, and $P_{44} = 3$ was assumed.

Because of the lack of additional measurements such as the nominal strain in the width direction, the Lankford ratios could not be calculated, and as a consequence an associated flow rule, enforcing normality of the incremental plastic strain tensor to the yield function, was assumed. This is achieved by setting $G_{12} = P_{12}$, $G_{22} = P_{22}$, and $G_{44} = P_{44}$ in Eq. (5).

To perform numerical analysis for further calibration, the constitutive law and the fracture model from Sect. 2 were implemented into Abaqus/Explicit using

Fig. 1 **a** Dog-bone specimen for uniaxial tensile tests; **b** engineering stress–strain curves of the 3.124 mm Ti–6Al–4V alloy sheet in rolling and transverse directions at slow (0.0254 mm/s) and fast (25.4 mm/s) loading speeds provided by Sandia National Laboratories



a VUMAT user subroutine (Abaqus 2016). Exploiting the symmetry of the dog-bone specimen with a large radius of curvature of $R = 14287.5$ mm in Fig. 1a, only one eighth of its geometry was discretized using three-dimensional brick elements with reduced integration (C3D8R) (see inserted figure in Fig. 3). It is emphasized that the Hosford–Coulomb fracture criterion is intended to predict the onset of fracture, not the propagation even though it can simulate propagation as a consecutive re-initiation. Therefore, a symmetric model of the specimen is allowed even though a finally separated piece showed an asymmetric fracture surface. Very fine elements ($0.1 \times 0.1 \times 0.1$ mm³) were used in the critical area of necking based on a convergence study as indicated by Dunand and Mohr (2010). Zero displacement boundary conditions were applied to the symmetry planes. Careful attention was paid to applying a velocity profile resulting in the same engineering strain versus

time relation at the position of the 25.4 mm extensometer as obtained from the experiments by SNL.

As mentioned before, the participants were allowed to report a lower and an upper boundary for the blind prediction. Therefore, two separate sets of hardening parameters were identified with the following methodology:

- The highest and lowest engineering stress–strain curves in RD at 0.0006/s from the set of tests provided by SNL are chosen. After converting each curve to true stress–plastic strain, the parameters of the Swift law (A , ϵ_0 , n) and the Voce law (k_0 , Q , β) are calibrated separately to each curve using a least square fit. As an example, the result for the highest case (specimen RD2) is illustrated in Fig. 2, showing a very good agreement.
- Due to their mathematical formulation (the Swift law based on a power function and the Voce law

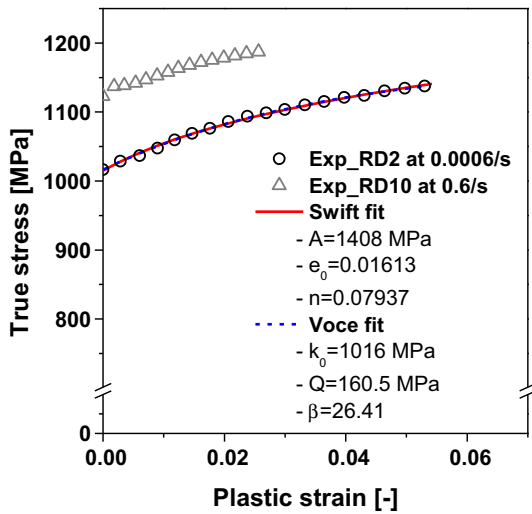


Fig. 2 True stress–plastic strain curve from the uniaxial tensile test that showed highest stress level at slow and fast loading speeds. Observe an excellent fit of the Swift (red) and the Voce (blue) law for the slow speed case

with an exponential function saturated to $k_0 + Q$, the two laws show a completely different response in the post-necking regime. Thus, a linear combination of the two functions [Eq. (8)] is sought to control the shape of the hardening curve after necking without changing its early part. The combination factor α is determined by an inverse method, optimizing it until the engineering stress–strain response at 0.0254 mm/s is accurately predicted up to fracture elongation. Assuming no dynamic effects for this low loading speed, rate hardening and thermal softening features are turned off, allowing for the exclusive determination of α . It has to be noted, as will be shown in Sect. 4, that this assumption underestimates the evolution of the strain rate and consequentially may lead to an overestimation of the parameter α . Figure 3 shows the results of the two calibrated α values for the upper and the lower boundary, based on the experimental scatter with the longest/shortest fracture elongation.

The strain rate sensitivity parameter C was calculated from the ratio of the true stress for the fast experiment ($\dot{\epsilon}_p = 0.6/s$) to the slow one ($\dot{\epsilon}_p = 0.0006/s$) at $\bar{\epsilon}_p = 0$. For this equivalent plastic strain, the strain rate effect can already be observed in the higher yield stress, while temperature softening has not yet come into play. The reference strain rate, as well as the isothermal limit, was chosen to be $\dot{\epsilon}_0 = \dot{\epsilon}_{it} = 0.0006/s$. The reference

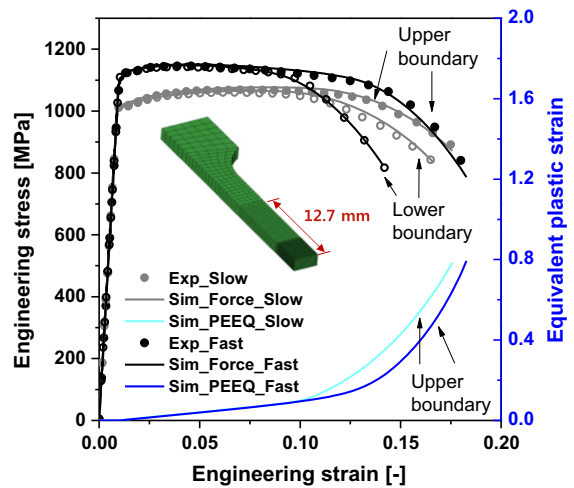


Fig. 3 Comparison of the engineering stress–strain curves from uniaxial tensile tests between experiments (dots) and simulations (lines) at 0.0254 (light grey) and 25.4 mm/s (black) for upper and lower boundary cases. The equivalent plastic strain is also shown as a function of the engineering strain for the upper boundary case. Inserted is the finite element model for a dog-bone specimen

and initial temperature were set to $T_r = T_0 = 293$ K. The two remaining model parameters, the adiabatic limit $\dot{\epsilon}_a$ and the temperature softening exponent m , were simultaneously optimized with an inverse method to match the engineering stress–strain curve for the fast loading case at 25.4 mm/s. Note that the uniqueness of two parameters was assured by confirming that no other combination could achieve a comparably satisfactory fit. Other general properties such as T_m , ρ , C_p , and η_k were taken from the MatWeb LLC webpage. Table 2 gives an overview of the calibrated parameters, and a comparison of the experimental and the simulated engineering stress–strain curves is given in Fig. 3. In addition, for the upper boundary, the evolution of the equivalent plastic strain $\bar{\epsilon}_p$ at the most deformed and thus critical element is also plotted. It reveals a positive effect of the strain rate on the ductility of the material and will be used in the calibration of the fracture model.

Besides the uniaxial tensile tests in RD and TD, SNL provided additional experimental data from V-notched rail shear tests to the participants (Fig. 4a, b), allowing for the examination of the material behavior under shear dominant loading. However, SNL stated in the challenge package provided to the participants that noticeable slippage of the specimens occurred during the experiments. Additionally, the test data contains non-negligible bending and rotation of fixtures due to the displacement measurement using LVDT

Table 2 Hardening model parameters of the 3.124 mm Ti–6Al–4V alloy sheet for the upper/lower boundary

A (MPa)	ε_0	n	k_0 (MPa)
1408/1393 (1380)	0.01613/0.01763 (0.01500)	0.07937/0.07955 (0.07300)	1016/1011 (1020)
Q (MPa)	β	α	C
160.5/147.2 (153.4)	26.41/24.94 (25.74)	1.400/1.200 (1.184)	0.01517/0.01605 (0.01908)
$\dot{\varepsilon}_a$ (1/s)	m	$\dot{\varepsilon}_0 = \dot{\varepsilon}_{it}$ (1/s)	$T_0 = T_r$ (K)
0.6000/1.000 (1.540)	0.7900/0.7400 (0.7882)	6.000E–4 (1.000E–3)	293.0
T_m (K)	ρ (kg/m ³)	C_p (J/kg K)	η_k
1900	4430	5.263E2	0.9000

Values in brackets are the results of the full calibration of the material

attached to the fixtures. Instead of trying to capture these very complex boundary conditions in a numerical simulation, a different modeling approach was pursued. An idealized engineering model was created, only discretizing the gauge section of the specimen (see inserted figure in Fig. 4c). The boundaries on both sides of the model were assumed not to rotate. This ideal boundary condition was compensated by scaling up displacement in the simulation such that the elastic part of the simulation could match that of the experiment. Figure 4c depicts the comparison of the force–displacement curve between the simulation and the experiment for the slow loading speed (0.0254 mm/s). $P_{44} = 3$, obtained based on the uniaxial tensile tests in RD and TD in the early step of the calibration, significantly over-estimated the overall force level. This suggests that the actual deformation resistance of the material under shear is much lower than that under tension in RD or TD. With an inverse method, $P_{44} = 3.9$ was determined. This observation is in accordance with the well-known fact that the Ti–6Al–4V alloy possesses poor shear strength. It was further verified that the change in P_{44} does not alter any simulation results for dog-bone specimens: in this geometry, shear stresses are only present in very limited regions and one order of magnitude lower than the axial stresses, thus of negligible influence.

3.1.2 Fracture model parameter identification

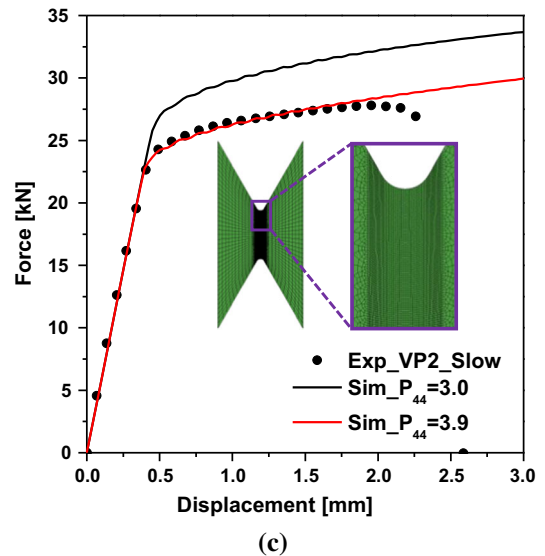
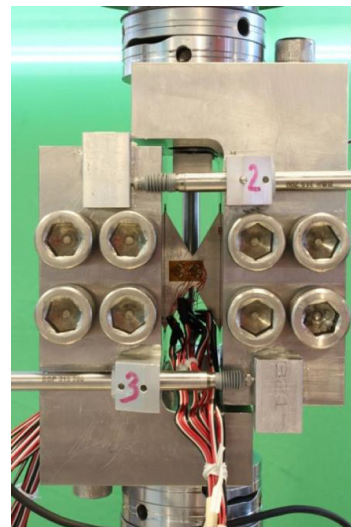
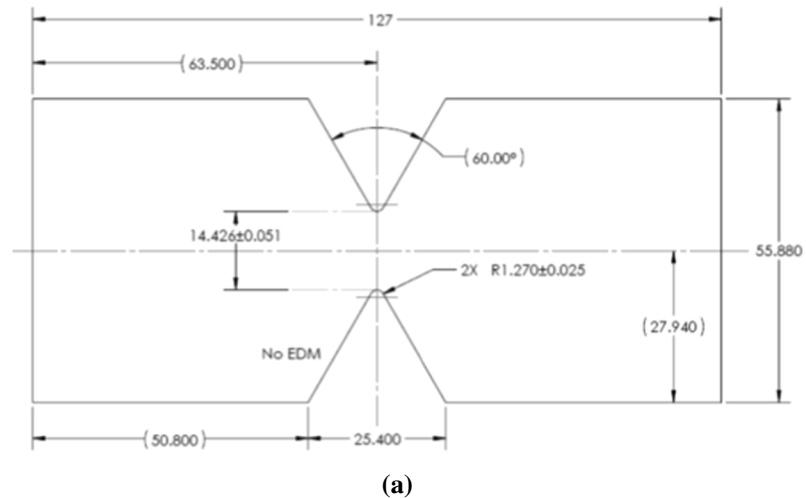
In the previous section, it was shown that after careful calibration the engineering stress–strain curves for

the uniaxial tensile tests could be accurately predicted for the slow and the fast case. Following a hybrid experimental–numerical approach (Dunand and Mohr 2010) to calibrate the fracture model, the loading history, comprising of the evolution of the stress triaxiality η , the Lode angle parameter $\bar{\theta}$, the equivalent plastic strain $\bar{\varepsilon}_p$, the strain rate $\dot{\bar{\varepsilon}}_p$, and temperature T , was extracted from the so-called critical element, the element exhibiting the highest equivalent plastic strain $\bar{\varepsilon}_p$ at fracture elongation. For the dog-bone specimen, it is located at the center on the mid-plane as indicated by a white dot on the necked cross section in Fig. 5b.

Due to the profound experimental and numerical uncertainties in the V-notched rail shear test, especially inconsistency of boundary conditions, it was not included in the calibration of the fracture model. Instead, the fracture parameters $\{a, c, n_f\}$ governing the shape of the fracture envelope were taken from the ICL's material database for a similar titanium alloy (Tancogne-Dejean et al. 2016). It has to be noted that without these parameters, an accurate calibration of the fracture model solely based on uniaxial tensile tests remains nearly impossible. Additional information from specimens with different geometries is required to fully calibrate the fracture model as further shown in Sect. 4.

The remaining parameters b and γ , controlling the overall strain to fracture and the strain rate dependence of the fracture model, were calibrated using the simulation results for the uniaxial tensile tests at different speeds in a two-step procedure:

Fig. 4 **a** V-notched shear specimen; **b** photo of a specimen installed in fixtures used for the V-notched rail shear test; **c** comparison of the force–displacement curve from slow V-notched rail shear test between an experiment (VP2, dots) and simulations for $P_{44} = 3.0$ (black line) and $P_{44} = 3.9$ (red line). Additionally, the finite element model of the specimen gauge section is shown



- First, the evolution of the stress triaxiality η , the Lode angle parameter $\bar{\theta}$, and the equivalent plastic strain $\bar{\epsilon}_p$ at the critical element for the slow speed case is extracted up to fracture elongation, which is assumed to be the instant of crack initiation (black solid line in Fig. 5a, b). The parameter b is then optimized with the strain rate effect switched off ($\gamma = 0$) such that the damage indicator D [Eq. (19)] is as close as possible to unity at the end of the loading path.
- Second, the loading paths are obtained from the fast case (red solid line in Fig. 5a, b), additionally including the evolution of the strain rate $\dot{\bar{\epsilon}}_p$. The strain rate sensitivity parameter γ is finally calibrated in the same way as b .

Figure 5a, b shows the calibrated fracture model for the upper boundary case in the three-dimensional space of η , $\bar{\theta}$, and $\bar{\epsilon}_p$ and its plane stress projection in the space of η and $\bar{\epsilon}_p$, respectively. Circular dots denote the predicted onset of fracture by the Hosford–Coulomb model. It is worth mentioning that the fracture parameters obtained from the lower boundary plasticity parameters yielded higher ductility than those from the upper boundary ones. Therefore, only one set of fracture parameters obtained from the latter was kept and applied to both the upper and lower plasticity cases in order to obtain the lowest possible response of the material based on the conservatism in a design standpoint. The fracture parameters are summarized in Table 3.

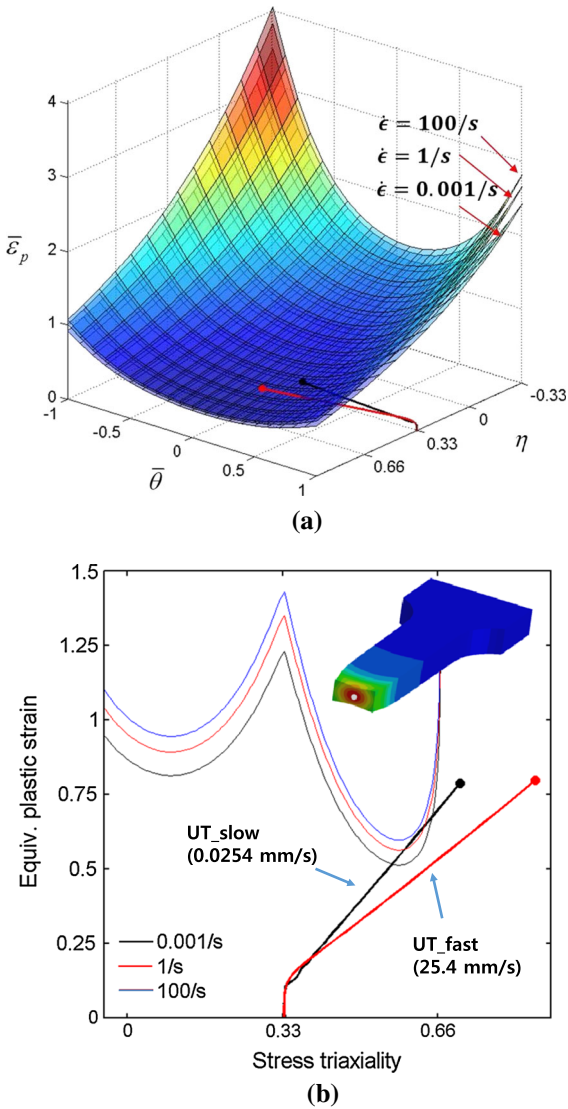


Fig. 5 Representation of the calibrated fracture model for the upper boundary case together with loading histories to failure of dog-bone specimens at slow (*solid black line*) and fast (*solid red line*) speeds. The predicted onset of fracture by the Hosford–Coulomb fracture model is indicated by solid dots. **a** three-dimensional envelopes for three exemplary strain rates; **b** two-dimensional loci for the plane stress condition in the space of the stress triaxiality η and the equivalent plastic strain $\bar{\epsilon}_p$

3.2 Numerical simulation of fracture challenge geometry

The geometry of the challenge specimen is shown in Fig. 6a. To easily report a crack path, notches, holes, and outer edges are named alphabetically. The

Table 3 Fracture model parameters of the 3.124 mm Ti–6Al–4V alloy sheet

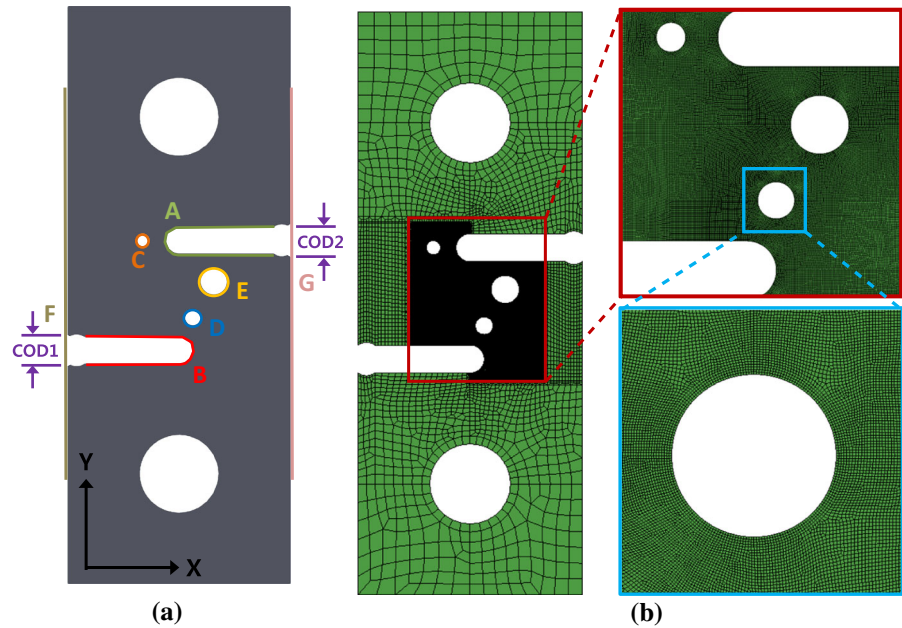
a	b	c	n_f	γ
1.15	1.22	0.0608	0.117	0.0142
(1.24)	(0.970)	(0.0500)	(0.0465)	(0.0800)

Values in brackets denote the parameters from the additional full calibration of the material

detailed dimensions of the specimen given in Fig. 10 of Boyce et al. (2016) were used for finite element modeling, not taking into account machining tolerances. Exploiting the geometrical symmetry, only half of the specimen thickness was modeled. Due to the time limit, a mesh convergence study for the challenge geometry was not pursued. Instead, the critical areas around the notches and holes were discretized with brick elements (C3D8R) of the same size and aspect ratio (1:1:1) as used for the dog-bone specimens to minimize a potential mesh size sensitivity. Fifteen elements were used over half the thickness. The resulting finite element mesh is shown in Fig. 6b. The total number of nodes and elements is about 820,000 and 760,000, respectively.

Two pins, considered to be an analytical rigid cylinder with the same radius as the upper and the lower hole of the specimen, were used to transmit the displacement to the specimen. A frictionless tangential interaction property was assigned between the specimen and the two rigid pins. A penalty contact algorithm was chosen instead of a kinematic one, because the nodes on the z-symmetric plane were involved in the boundary condition as well. The upper pin was fixed, and the lower pin was pulled down at 0.0254 mm/s for the slow case and at 25.4 mm/s for the fast case as determined by SNL. The velocity was accelerated from zero to these target values for one tenth of total simulation time that resulted in the translation of the lower pin of about 6.5 mm, which is consistent with a usual experimental condition. The cross-head is indeed accelerated, and its displacement is not all transmitted to the specimen in the early stage due to the compliance of mechanical systems in the testing machine (note that the actual velocity profile of the lower pin in challenge experiments was not provided by SNL). This also ensures that unnecessary noise in the quantity of interest such as the reaction force at the fixed upper pin is

Fig. 6 **a** Geometry and designations of the challenge specimen; **b** finite element mesh of the challenge specimen



removed by smooth transition from elastic to plastic domain.

Crack initiation was modeled using the element deletion technique, and propagation was considered to be a consecutive crack re-initiation. In total, four cases were simulated consisting of the upper and lower boundary cases at slow and fast loading speeds.

3.3 Comparison of challenge geometry experiments and simulations

Experiments on the challenge geometry were performed by SNL, and the results were unveiled after all participants had submitted their blind prediction of the crack path and the force–COD1 curve. Two independent labs at SNL, the Solid Mechanics Lab and the Materials Mechanics Lab, tested a total of 11 samples for the slow loading condition and 8 samples for the fast loading condition. All but one sample in the slow test failed by the path B–D–E–A. SNL pointed out that the outlier case (A–C–F) was attributed to the pronounced non-flatness of the specimen.

3.3.1 Crack initiation and propagation

All four simulations performed by the MIT team, both upper and lower boundary cases at slow and fast speeds,

consistently predicted a crack path of B–D–E–A, agreeing with the experimental results. Figure 7 visualizes a representative deformation and crack development for the slow upper boundary case by means of the damage indicator. In the early stage, plastic deformation results mainly from stress concentration around notches and holes. The ligament between A and C is deformed by tension whereas two ligaments between B and D and D and E undergo combined shear and tension. Additional global displacement leads to a localization of the deformation in the narrow band of sheared ligaments. This is due to the material's weak deformation resistance under in-plane shear. The two ligaments finally fail almost at the same time. Using a high-speed camera (20,000 fps), the team from the University of Texas at Austin performed follow-up experiments for the slow case. They revealed that the upper ligament between D and E breaks first, followed almost immediately by the breakage of the B–D ligament (Gross and Ravi-Chandar 2016). This interesting observation is captured by the presented modeling approach as shown in Fig. 8. The element on the boundary of the hole D in the ligament between D and E on the mid plane (red circle) is deleted first, indicating the onset of fracture. The two sheared ligaments crack completely in the next frame. This phenomenon was also observed in the simulation of the fast loading case, but it needs to be further validated experimentally. Finally, the combination of

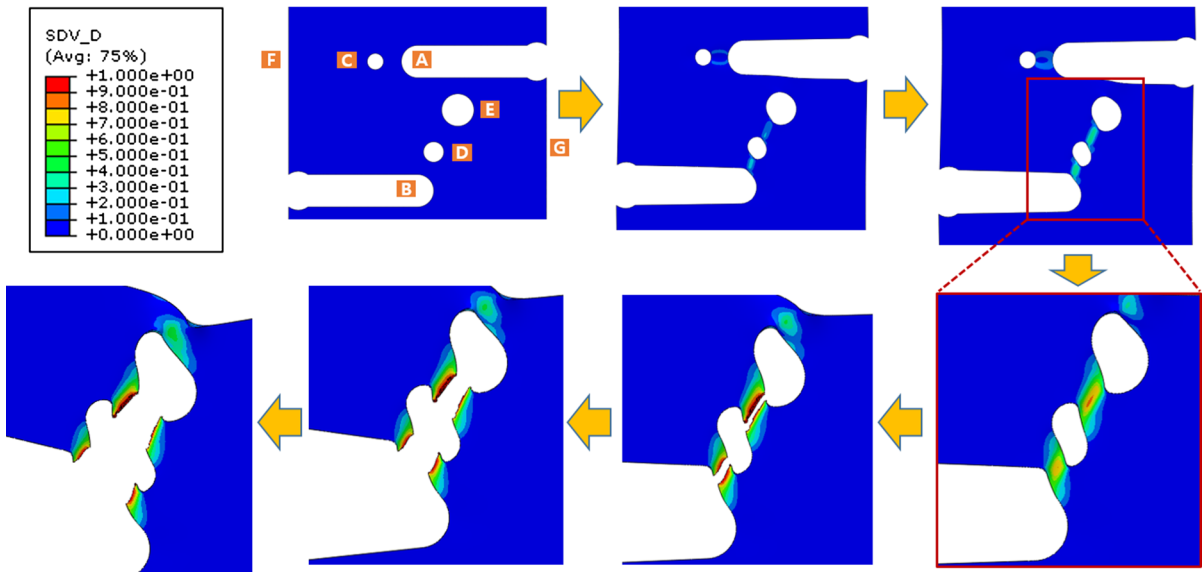


Fig. 7 Sequence of damage accumulation and crack development for the slow upper boundary case with $P_{44} = 3.9$ on the mid-plane (contour is for the damage indicator D interpreted as percentage of ductility that material point already consumed)

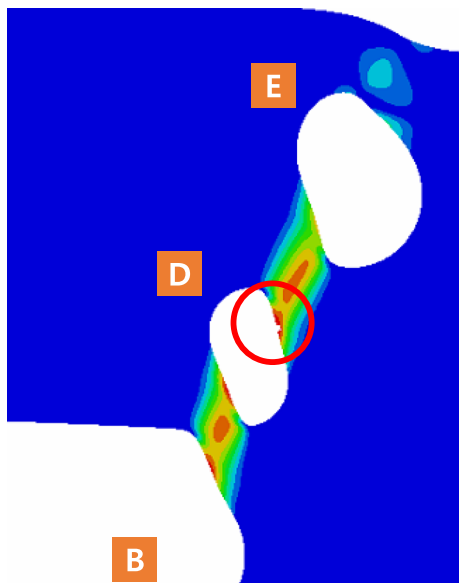


Fig. 8 Distribution of the damage indicator D for the slow upper boundary case when the first element is deleted. This shows that fracture initiates on the lower boundary of the ligament between D and E on the mid-plane

bending and tension applied to the remaining ligament between E and A leads to ultimate failure.

For comparison, the sequence of deformation assuming a von Mises yield surface ($P_{44} = 3.0$), is also

simulated and shown in Fig. 9. The increased deformation resistance under shear stress favors necking in the $A-C$ ligament. As a result, the crack initiates there and propagates to the backside edge F . This finding re-emphasizes the importance of a thorough material characterization under shear.

However, the use of an anisotropic Hill’48 yield criterion is not the only solution and may not be correct, as P_{44} ends up also influencing the yield stress under tension in other directions, e.g. 45° direction (DD). [Bai and Wierzbicki \(2008\)](#) showed that Al2024-T351 despite its isotropy could not be entirely described with the J2 plasticity theory. They proposed a new plasticity model that has a flow dependence on the stress triaxiality η and the Lode angle parameter $\bar{\theta}$, thus capturing a weak shear strength without altering the nature of isotropy.

3.3.2 Force–COD curve

Figure 10 shows the comparison of the force–COD1 curves between the simulations for the upper (solid red line) and the lower boundary case (solid blue line) and all experiments showing a $B-D-E-A$ crack path (grey lines). The prediction made by other participants can be found in Fig. 22 of [Boyce et al. \(2016\)](#).

The overall shape of the curves and the force levels are predicted with a high level of accuracy. To

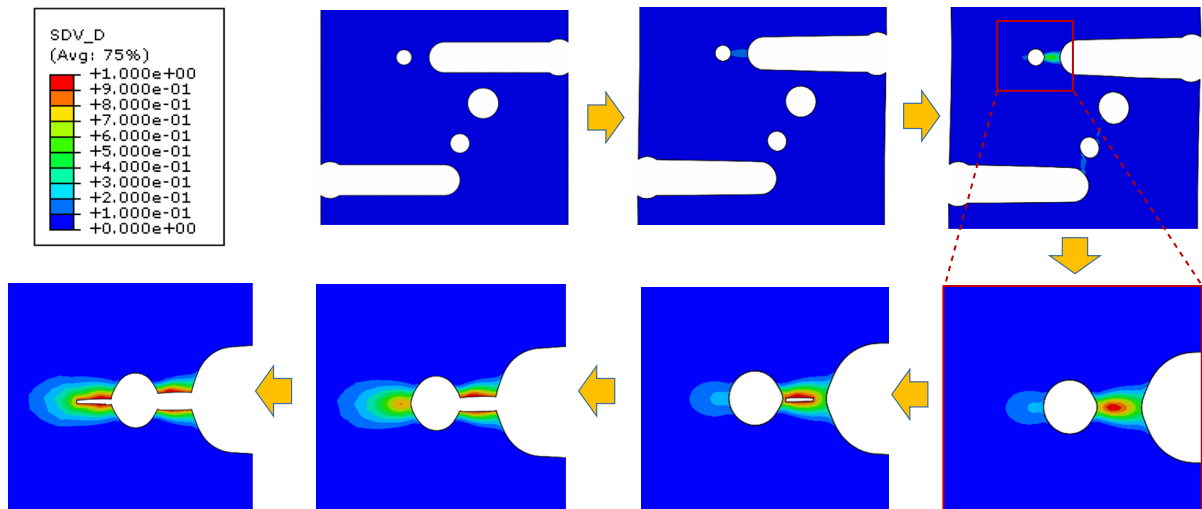


Fig. 9 Sequence of damage accumulation and crack development for the slow upper boundary case with $P_{44} = 3.0$ on the mid-plane

be more quantitative, the force level at $COD1 = 1$ and 2 mm are overestimated by 7.02 (5.34%) and 2.10% (0.65%) for the slow speed and by 5.66 (4.15%) and 2.07% (0.16%) for the fast speed in the case of the upper (lower) boundary simulation. The maximum force is also slightly over-predicted by 6.30 (3.60%) and 2.22% (0.07%), respectively. This slight overestimation might have originated partially due to incomplete description of plasticity and dimensional discrepancy between actual specimens and the finite element model.

However, the $COD1$ at crack initiation, which is identified by a sudden drop in force, is overshoot by a non-negligible amount for the slow case. The lower and the upper boundary case over-predict the $COD1$ by 47.4 and 57.8%, respectively. In contrast, the fast case is predicted more accurately. The upper boundary prediction overshoots by 20.2%, and the lower boundary prediction is within the experimental scatter.

A close examination of the results reveals that the poor prediction of the $COD1$ at crack initiation is caused by an inaccurate calibration of not only the fracture model but also the plasticity model. Three main aspects are:

- First, the dependency of fracture loci on η and θ , represented by the parameters $\{a, c, n_f\}$, relied entirely on the material database. Similar alloys can possess entirely different fracture properties depending on detailed plasticity properties, caused by different manufacturing process and heat treat-

ment. The only type of fracture experiment used in the calibration process was the dog-bone shaped specimen whose stress state lies away from the shear-dominant state revealed to be critical in the challenge specimen. The V-notched rail shear tests without slippage would have led to more accurate description of ductility of the alloy.

- Second, for the slow case the effect of the strain rate cannot be completely ignored once necking takes place. Recall that the determination of the weighting factor α in Sect. 2.2 was solely based on the engineering stress–strain curve for the slow speed with the rate sensitivity and thermal softening turned off. The calibration of α , m , and $\dot{\epsilon}_a$ should have been performed simultaneously for the engineering stress–strain curves for both the slow and the fast speed, as will be shown in Sect. 4.
- Third, ductile fracture is a local phenomenon as a consequence of significant plasticity. Therefore, plasticity in large deformation i.e. the hardening curve in the post necking regime plays a very important role. It was pointed out by many researchers (e.g. Pack et al. 2014; Marcadet and Mohr 2015) that the plasticity calibration based on a dog-bone specimen does not allow for an accurate prediction of large deformation in other specimen geometries or structural components. Necking in a dog-bone specimen is governed mainly by material imperfection rather than the geometry itself due to its parallel gauge section. Instead, a flat specimen with

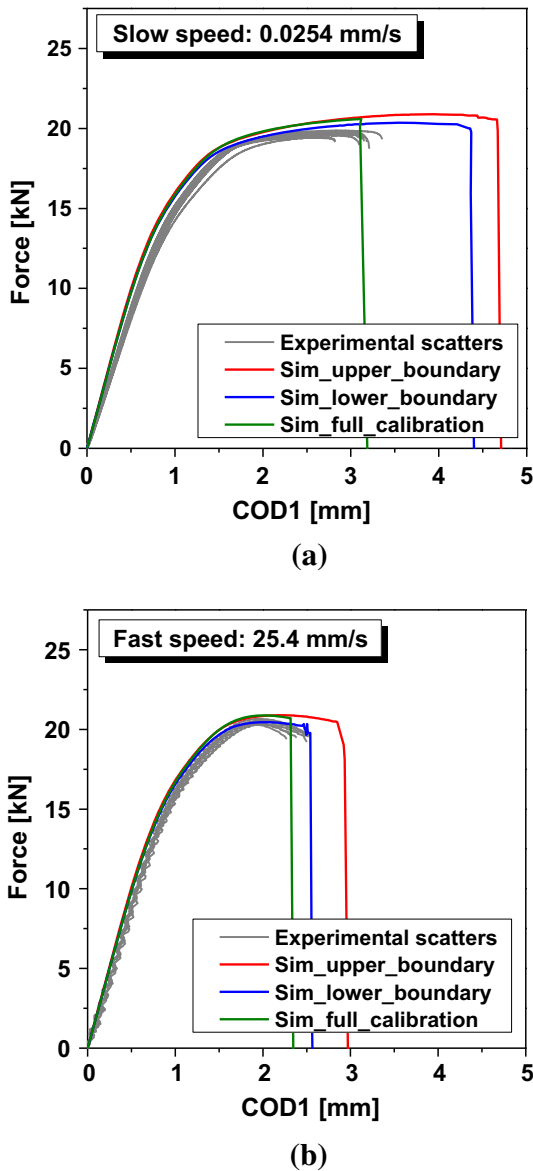


Fig. 10 Comparison of force–COD1 curves between experiments and simulations: **a** at the slow speed; **b** at the fast speed

symmetric circular cutouts (a notched tension specimen) is recommended.

4 Full characterization of plasticity and fracture properties based on additional experiments

After the blind round robin, SNL provided the ICL with a leftover sheet from the challenge to conduct additional experiments and fully characterize the Ti–

6Al–4V alloy. This section introduces a new testing program, corresponding numerical simulations, and a more advanced calibration technique to characterize the material in a wide range of stress states and strain rates.

4.1 Experimental program performed at MIT

4.1.1 Experimental setup

It can be seen from the challenge geometry that there are two competing fracture mechanisms: tensile fracture along A–C–F and shear-dominant fracture along B–D–E–A. Hence, the additional testing program consists of four types of specimens extracted mainly in RD of the sheet (Fig. 11) that cover a wide range of stress state probable in the challenge specimen including uniaxial tension, plane strain tension, and pure shear:

- Uniaxial tension (UT) specimens with a 40 mm long and 10 mm wide gauge section. These were extracted at 0°, 45°, and 90° with respect to the sheet rolling direction (RD, DD, and TD, respectively).
- Notched tension specimens (NT) with a 20 mm wide gauge section, which is reduced to a width of 10 mm in the center by circular cutouts. Two different notch radii of $R = 20$ mm (NT20) and $R = 6.67$ mm (NT6) were considered.
- Specimens with a central hole (CH). These specimens with a 20 mm wide gauge section feature an 8 mm diameter hole in the center.
- Smiley shear (SH) specimens with the 20 mm width and two shape-optimized gauge sections obtained by the methodology described in Roth and Mohr (2016).

The SH specimens were cut by a wire EDM, while all other geometries were machined with a CNC end mill. A random speckle pattern was applied to the surface of specimens prior to testing to allow for the accurate measurement of the relative displacement between two points on the shoulders of specimens (blue dots in Fig. 11), using digital image correlation (DIC) (VIC2D, Correlated Solutions, SC). The initial distance between these points was 8 mm for UT specimens and 30 mm for NT, CH, and SH specimens.

All experiments were carried out on an Instron 8080 hydraulic testing machine equipped with custom-made

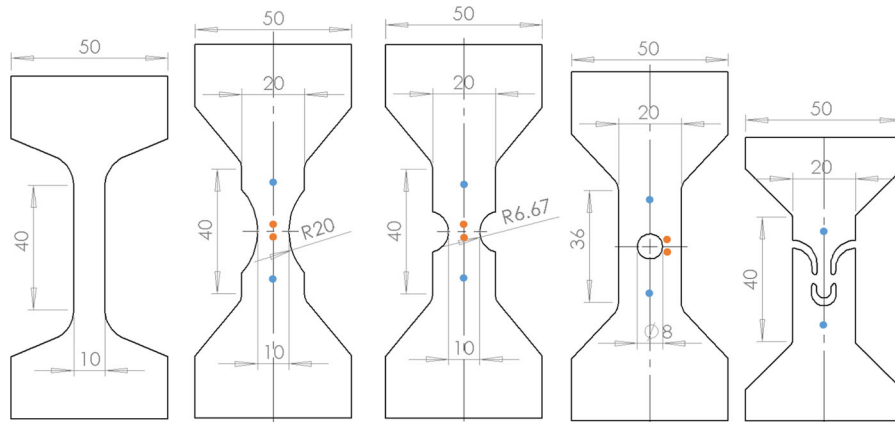


Fig. 11 Specimens for the additional testing program at slow and fast loading speeds. From left to right, specimens for: uniaxial tension (UT), notched tension with R20 cutouts (NT20), notched tension with R6.67 cutouts (NT6), tension with a D8 central hole

(CH), and smiley shear (SH). *Blue solid dots* highlight the position of the virtual extensometer for relative displacement and speed measurements; *red solid dots* highlight the position for local axial strain measurements

high pressure clamps. To be consistent with the experiments performed by SNL, two different testing speeds were considered:

- Low speed, with a cross-head velocity of 2.4 mm/min (0.001/s) for UT (in all three directions) and 0.4 mm/min for NT, CH and SH specimens. Images for DIC were obtained using a 1300×1030 pixel monochrome camera with an acquisition frequency of 1 Hz.
- High speed, with a cross-head velocity of 2400 mm/min (1/s) for UT (only in RD) and 400 mm/min for NT and CH specimens. The images for DIC were acquired at a frequency of 1000 Hz using a high speed camera (Phantom 7.3, Vision Research) with a resolution of 800×600 pixels. The high speed camera was triggered by a TTL pulse from LabView's Signal Express, thus assuring the synchronization of data and images.

All experiments were performed at least twice for each loading speed to ensure repeatability.

4.1.2 Experimental results

The true stress–strain curves measured from UT experiments in RD, DD, and TD for the strain rate of 0.001/s are shown in Fig. 12. The material exhibits a much weaker response in DD, for which the flow stress is approximately 7% lower than for the other two direc-

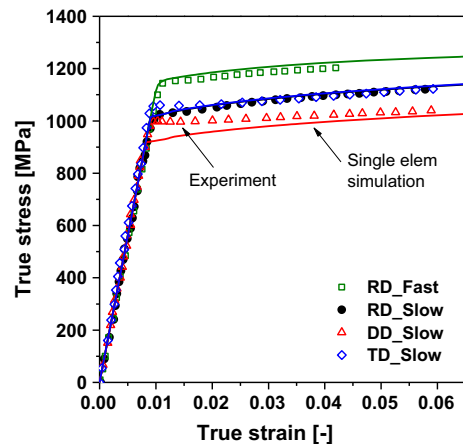
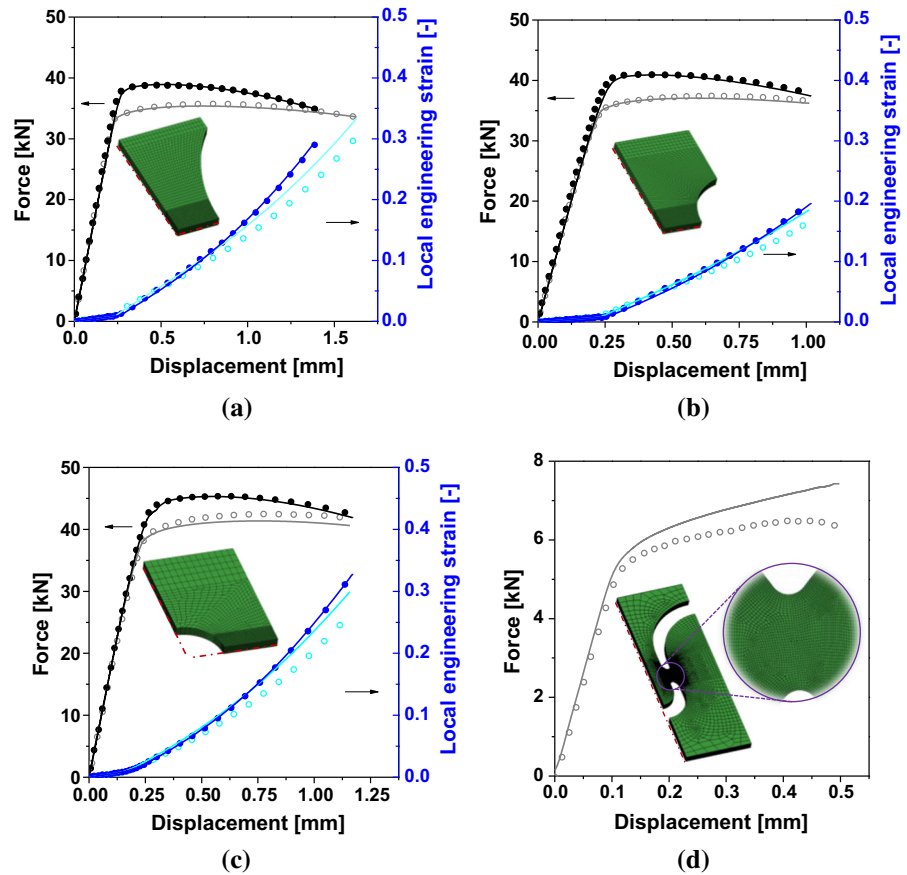


Fig. 12 True stress–strain curves from uniaxial tensile tests in three different directions (RD, DD, TD) at the slow speed (0.001/s) and in RD at the fast speed (1/s). *Symbols* denote experimental results, while *solid lines* are from single element calculations

tions. This important information was not included in the challenge package provided by SNL. The curves in RD and TD are very similar and match those at 0.0006/s in Fig. 1b. The corresponding Lankford ratios (i.e. plastic strain ratios or r-values) were calculated from plastic strains in the axial and the width direction,

$$r = \frac{d\varepsilon_w^p}{d\varepsilon_{th}^p} = -\frac{d\varepsilon_w^p}{d\varepsilon_w^p + d\varepsilon_{ax}^p} \quad (20)$$

Fig. 13 Comparison of the force–displacement curve and the evolution of local axial engineering strain for **a** NT20, **b** NT6, **c** CH, and **d** SH specimen between experiments (*dots*) and simulations (*solid lines*) at slow (*grey and cyan blue*) and fast (*black and navy blue*) speeds. Inserted figures show the finite element discretization



resulting in $r_0 = 1.38$, $r_{45} = 3.76$, and $r_{90} = 2.88$. Figure 12 also shows the effect of the strain rate for a UT specimen in RD. For a strain rate of about 1/s, it exhibits an 11 % higher yield stress than for a strain rate of 0.001/s.

Figure 13 shows the results of NT and CH experiments at slow and fast speeds as well as SH experiments at the slow speed. The onset of fracture was determined from the steep drop in the force–displacement curve. It is worth mentioning that all experiments showed an excellent repeatability in both the force–displacement curve and the onset of fracture. Only for the NT20 specimens, a noticeable deviation was observed in the onset of fracture at the slow speed. Within the framework of this article, the experiment with the shorter displacement to fracture was used, which can be regarded as a lower boundary.

In all experiments, a force maximum is observed before the onset of fracture, which indicates the duc-

tile nature of fracture. However, the shape of the curve changes with the loading speed. The fast case shows a significantly higher maximum force (positive strain rate sensitivity), which occurs much earlier in the displacement than for the slow case. This is followed by a relatively rapid decrease in the force until the onset of fracture. Note that in spite of different loading speeds, the same specimen geometry exhibits the almost identical displacement to fracture, again with the exception of the NT20.

To gather deeper insight into the deformation behavior, an axial surface engineering strain was measured with a 2 mm virtual extensometer lying on the longitudinal axis of symmetry for NT specimens and 1 mm away from the boundary of the central hole for CH specimens, as depicted in Fig. 11. These measurements are plotted on the secondary axis of Fig. 13. All cases but NT20 show an increase in the measured local engineering strain with increasing loading speed.

4.2 Full calibration of plasticity model

4.2.1 Numerical simulations and parameter identification

All simulations were carried out using Abaqus/Explicit with the aforementioned constitutive model implemented through VUMAT. Taking advantage of the symmetries of the specimens, only one eighth was modeled with C3D8R elements for NT20, NT6, and CH specimens whereas a quarter was discretized for the SH specimen. The length of each finite element model corresponds to half the global extensometer, so that the measured displacement history can be directly applied to the nodes on the upper boundary of the model. Critical areas of the specimens were meshed with an element edge length of about 0.1 mm and eight elements through half the thickness.

The parameters for the plasticity model were determined as follows:

- The previously identified P matrix ($P_{12} = -0.5$, $P_{22} = 1.0$ and $P_{44} = 3.9$) for the yield function is maintained. Instead, this is validated by performing single element calculations. More detailed explanation is given in Sect. 4.2.2.
- Complete uniaxial tensile tests in three different in-plane directions reveal a much softer flow stress in DD. This tendency is different from the Lankford ratios. Thus, a non-associated flow rule is chosen. Using the measured Lankford ratios in conjunction with the analytical relationships from the non-associated flow rule,

$$G_{12} = -\frac{r_0}{1+r_0}, \quad G_{22} = \frac{r_0}{r_{90}} \frac{1+r_{90}}{1+r_0} \text{ and}$$

$$G_{44} = \frac{1+2r_{45}}{r_{90}} \frac{r_0+r_{90}}{1+r_0},$$

$$G_{12} = -0.58, \quad G_{22} = 0.78 \text{ and } G_{44} = 5.29. \quad (21)$$

- Because the same hardening law as in Sect. 3 is used, the Swift parameters $\{A, \varepsilon_0, n\}$ and the Voce parameters $\{k_0, Q, \beta\}$ are determined from two separate fits to the true stress–plastic strain curve at 0.001/s.
- The weighting factor α of the combined Swift–Voce strain hardening law together with the strain rate sensitivity C , the temperature softening exponent m , and the adiabatic limit strain rate $\dot{\varepsilon}_a$ are then optimized through inverse analysis for NT20 at slow

and high speeds, for which large plastic strains are attained.

- The isothermal limit strain rate is chosen to be $\dot{\varepsilon}_{it} = 0.001/s$, which corresponds to the strain rate of the slow UT experiments. Otherwise, all parameters from Sect. 3.1.1 are kept. Table 2 summarizes the newly optimized parameters in brackets.

4.2.2 Comparison between experiments and simulations

Normally, the yield stresses under uniaxial tension in RD, DD, and TD and the equi-biaxial yield stress are used to uniquely determine the P matrix. However, the absence of this complete set of data in Sect. 3 led to P_{44} being inversely identified based on the V-notched rail shear test. With the true stress–strain curve in DD available from the additional testing program, single element calculations of uniaxial tension in three different directions were performed and compared with experimental results as illustrated in Fig. 12. A satisfactory agreement in DD validates not only the previous calibration but also the use of the Hill'48 quadratic yield function for the Ti–6Al–4V alloy. It can be concluded that a weak deformation resistance under shear loading originates from anisotropy rather than the Lode angle dependency. Remaining discrepancies are attributable to the difference in the instantaneous hardening modulus between RD and DD. This anisotropic hardening could be taken into account by a more complex plasticity model such as the one proposed by [Stoughton and Yoon \(2009\)](#).

Figure 13 demonstrates that the chosen plasticity model with a new calibration is accurate to capture the important features of the specimens tested in Sect. 4.1.1. Overall, the force–displacement curves for NT and CH specimens were predicted with a high level of accuracy. Not only the displacement at maximum force but also the rate at which the force decreases was predicted very precisely. A minor over-estimation for the SH specimen is partially due to the limitation of the Hill'48 quadratic yield function. Here, a more accurate prediction of the force level could be achieved for $P_{44} = 4.4$, but at the same time this would deteriorate the accuracy of the true stress–strain curve in DD. To address this, a more elaborate construction of the yield function would be required. It is also noted that the experimental curve shows a substantial softening at the end due to the formation of a narrow shear band,

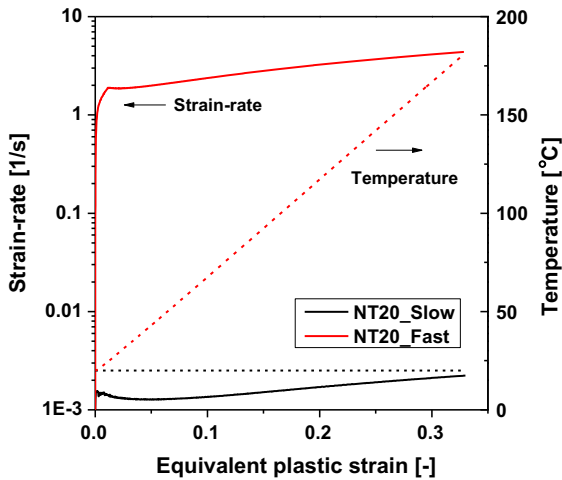


Fig. 14 Evolution of the strain rate and temperature as a function of the equivalent plastic strain at the critical element of the NT20 specimen at slow and fast speeds

which could not be simulated by the current finite element model.

On the other hand, excellent agreement was achieved in the evolution of the local engineering strains for the fast loading cases, while they were slightly over-predicted for the slow cases. Nevertheless, this indicates that necking, the phenomenon preceding ductile fracture, was modeled accurately. It is worth noting that the local engineering strains at two different speeds evolve differently early in the experiment. This behavior, leading to the curves intersecting each other, was captured in the simulations (navy and cyan blue lines in Fig. 13).

4.3 Full calibration of fracture model

With the calibration and validation of the plasticity model completed, the loading path to fracture was extracted from the critical element in each simulation using the methodology described in Sect. 3.1.2. Figure 14 gives an example of the evolution of the strain rate and temperature as a function of the equivalent plastic strain at the critical element of the NT20 specimens. It can be observed that the strain rate increases by approximately a factor of 5 over the initial strain rate. For this reason, it is important to take into account the effect of strain rate hardening even for the slow case. The temperature remains constant for the slow case, while it increases by approximately 150°C for the fast case. However, a thermocouple was not used in the

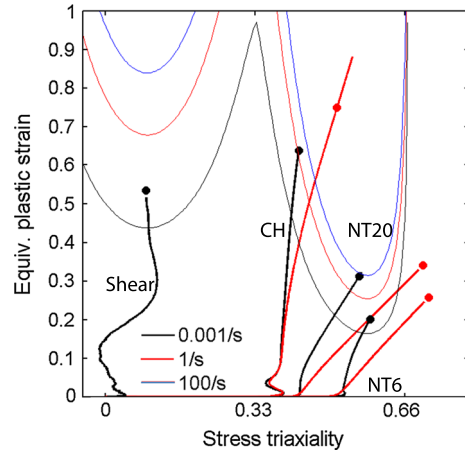


Fig. 15 Loading paths to fracture for the specimens included in the additional testing program at slow (*black lines*) and fast speeds (*red lines*). On each curve, the fracture strain predicted by the rate-dependent Hosford–Coulomb model is indicated by *solid dots*. Additionally, the fracture loci at three different strain rates are illustrated

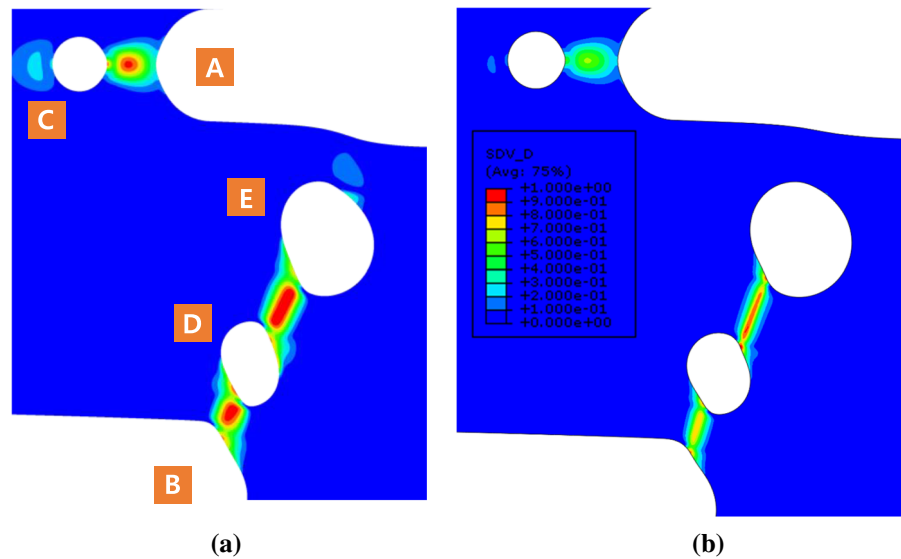
experiment, so quantitative comparison of temperature was not performed.

Figure 15 shows the evolution of the equivalent plastic strain $\bar{\epsilon}_p$ against the stress triaxiality η for all specimen geometries. The slow cases are drawn in solid black lines and the fast cases are plotted with solid red lines. The predicted onset of fracture by the calibrated rate-dependent Hosford–Coulomb fracture model is denoted by solid dots. An accurate prediction was achieved for the parameters $a = 1.24$, $b = 0.97$, $c = 0.05$, $n = 0.0465$, and $\gamma = 0.08$. In addition, the fracture loci for the strain rates of $\dot{\bar{\epsilon}}_p = 0.001/s$ (black W-shaped curve), $\dot{\bar{\epsilon}}_p = 1/s$ (red), and $\dot{\bar{\epsilon}}_p = 100/s$ (blue) are illustrated. Note that the loading path evolves differently for the same geometry at different loading speeds. This is mainly due to the change in hardening behavior at different strain rates and temperatures. For slow cases, the maximum force occurred at about half the displacement to fracture, while for fast cases, it was observed significantly earlier, which was followed by a prolonged decrease in the force level. In addition to that, due to the limited accuracy in predicting the behavior of the SH specimen, the strain to fracture has to be considered a lower boundary.

5 Discussion

Following the full calibration based on the comprehensive experimental program, both the plasticity model

Fig. 16 Contour plot of the damage indicator D for the challenge specimen on the mid-plane just before crack initiation at **a** the slow speed and **b** the fast speed. Observe the formation of a shear band



and the fracture model were applied to the challenge problem, using the same numerical method as described in Sect. 3.2.

5.1 Improvement in prediction by full characterization

The crack path remained unchanged as B–D–E–A, and the sequence of deformation, localization, and crack development were very similar to what was observed in the initial blind simulation (see Fig. 7). Figure 16 shows a damage distribution on the mid-plane right before crack initiation for slow and fast speeds. It is observed that deformation is localized along a narrow band in both cases. The width of the localization band in the fast case is much narrower than in the slow case. This is because the strain rate within the band for the fast case is well above the adiabatic limit $\dot{\epsilon}_a$. As a result, the temperature rise and the consequent softening are more pronounced, leading to more localized deformation. Both cases show higher damage accumulation in the ligament between D and E than in the ligament between B and D. Figure 17 clearly demonstrates that the ligament between D and E breaks earlier for both the slow and the fast case, which is in line with the experimental observation for the slow case by Gross and Ravi-Chandar (2016) (Fig. 17c). It is stressed that two ligaments fracture almost with no time elapse, which required a very tiny field output interval to capture the moment.

The force–COD1 curves predicted by the new simulations are plotted with green solid lines in Fig. 10. The force level is still slightly over-predicted, but the shape of the curves agrees very well with the experimental data. A great improvement is obtained in the COD1 at crack initiation. Its value at both loading speeds lies well within the experimental scatter. Compared to the fracture loci determined in Sect. 3.1.2 (Fig. 5b), a new fracture calibration revealed a significantly lower ductility at 0.001/s with a much higher strain rate sensitivity (Fig. 15). This made it possible to improve the COD1 at crack initiation for the slow case without worsening the prediction for the fast case. It has to be noted that all simulations already slightly overestimate the slope in the elastic region. This might have been caused by the compliance of the cylindrical connector pins placed in the lower and upper holes of the specimens. A simple analogy can be made with two springs in series, where the overall stiffness is less than that of a single spring. Li et al. (2010) showed a possible strong influence of the machine stiffness on the force–displacement curve in their work.

5.2 Investigation of loading path at critical points

Figure 18 shows the loading path to fracture for two critical elements for the slow (black) and the fast case (red). The solid dots represent the predicted onset of fracture from the model. Fracture starts in the center of

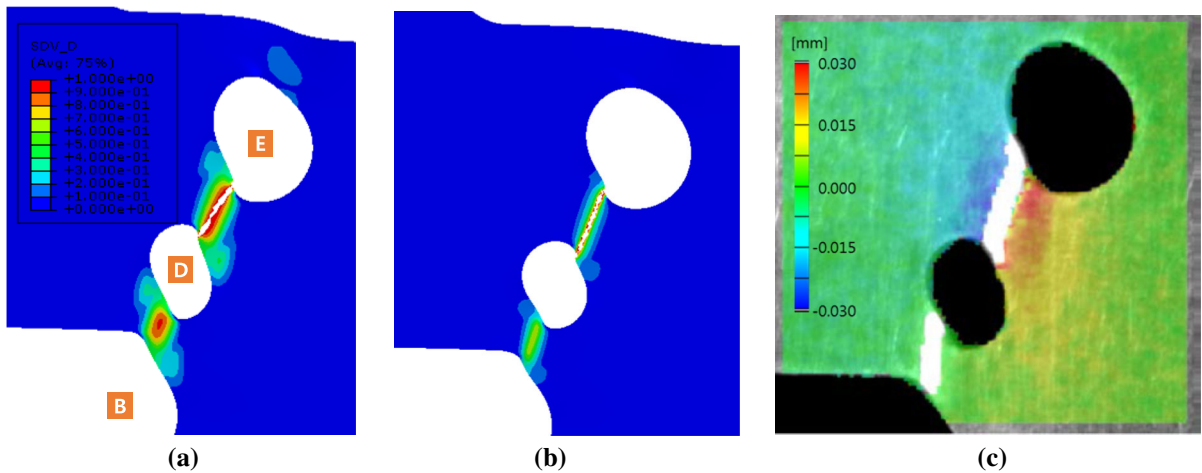


Fig. 17 Moment of fracture of the D–E ligament ahead of the B–D ligament: **a** finite element simulation for the slow speed (contour plot of the damage indicator D just after the breakage

of the D–E ligament); **b** simulation for the fast speed; **c** experimental evidence observed by the team of the University of Texas at Austin (adapted from Fig. 90b in Boyce et al. 2016)

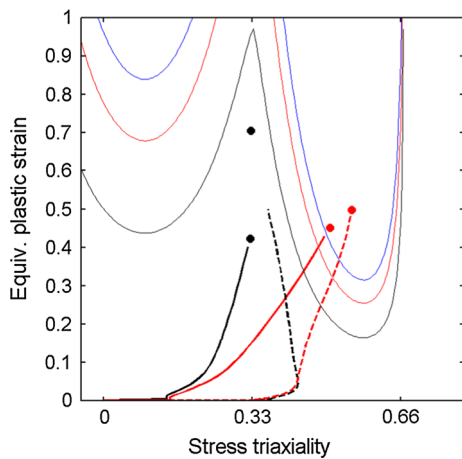


Fig. 18 Loading histories at two critical points in the D–E ligament for slow (black) and fast speeds (red); one from the element located in the center (solid line) and the other from the element located on the lower boundary (dashed line)

the D–E ligament on the mid-plane for the slow case with a stress state evolving from pure shear ($\eta = 0$) to uniaxial tension ($\eta = 1/3$) (see black solid line). This is in contrast to the blind prediction in Fig. 8. In the fast case, fracture commences from the lower boundary of the D–E ligament on the mid-plane with a stress state changing from uniaxial tension to plane strain tension ($\eta = 1/\sqrt{3}$) (see red dashed line). When examining an element from the center of the D–E ligament on the mid-plane (red solid line), one can observe that it fails

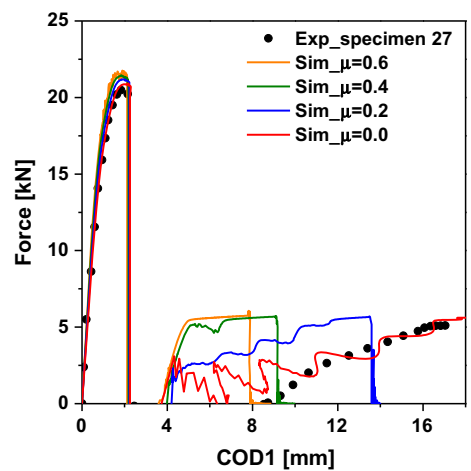


Fig. 19 Comparison of force–COD1 curve between the sample 27 and simulations with four different friction coefficients all the way to ultimate failure of the challenge specimen

almost at the same time and in a similar final stress state. In general, the onset of fracture occurs under a combined shear and tensile stress state for both speeds.

5.3 Effect of friction between pins and challenge specimen

There have been a number of discussions among participants over what boundary conditions are appropriate to simulate the challenge problem such as modeling of

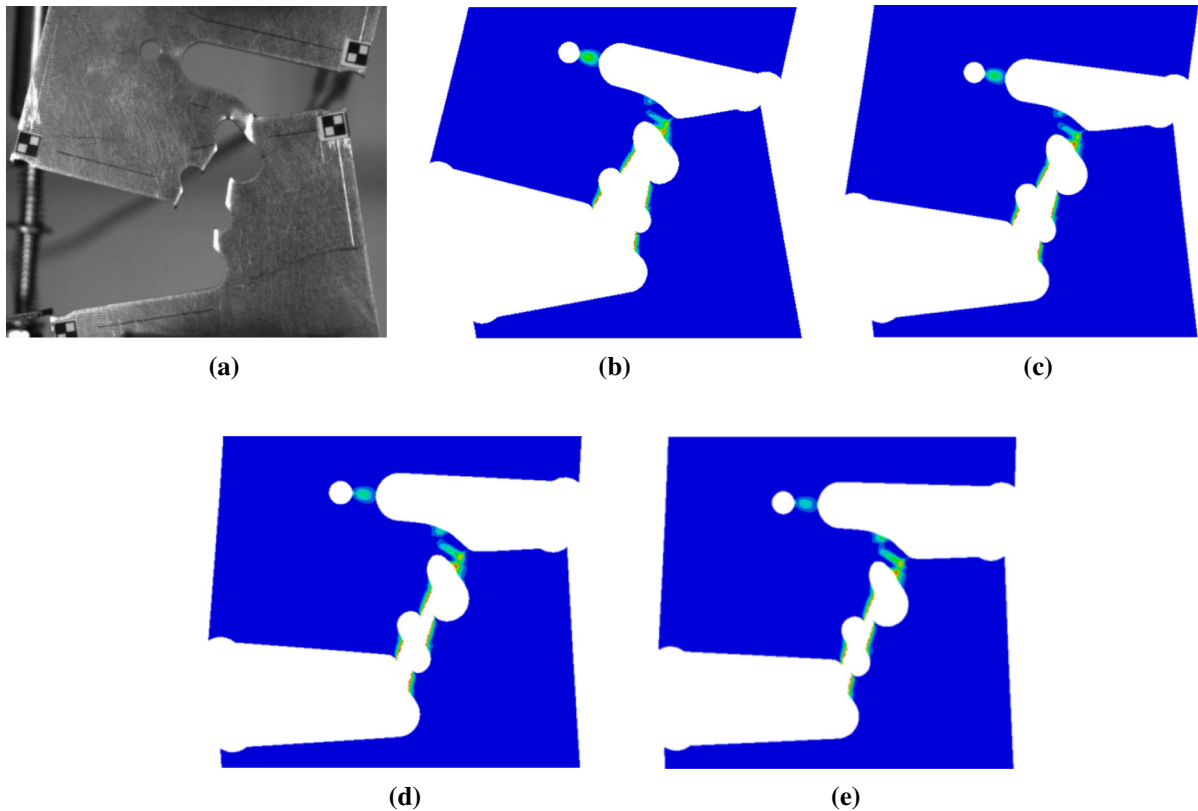


Fig. 20 Deformed configuration of the challenge specimen right before ultimate failure (*contour plot* indicates the distribution of damage indicator): **a** experiment (sample 27); **b** $\mu = 0.0$; **c** $\mu = 0.2$; **d** $\mu = 0.4$; **e** $\mu = 0.6$

pins, friction between pins and the specimen, etc. This section is devoted to partially addressing the issue of friction coefficients.

The team E from France performed DIC analysis on the video clip for the challenge sample 27 at the fast speed provided by Sandia after the challenge ended. This allows for the comparison of the force–COD1 curve between experiment and simulation even after the COD gauge jumps off the sample due to catastrophic crack propagation from B to E and subsequent vibration. The comparison with the simulations with four different friction coefficients all the way to the ultimate failure (breakage of the E–A ligament) is shown in Fig. 19. It is clearly seen that the friction coefficient does not have a noticeable effect on the COD1 at the first crack initiation. It slightly increases the overall force level. However, its influence becomes significant in the later stage. Increasing friction shortens the COD1 at the complete failure of the specimen. Frictionless condition tracks the experimental result the best. The

oscillation on the force prediction is attributed to not entirely removing the inertia effect by using explicit time integration scheme and mass scaling. Figure 20 compares the deformed shape of the challenge specimen just before ultimate failure. The case with zero friction matches the experimental shape most accurately. With no doubt, a higher friction coefficient prevents relative rotation between two material blocks connected to the E–A ligament more effectively, which changes a dominant stress state in the E–A ligament. Therefore, the COD1 at the complete failure is highly affected by friction. A simple qualitative analysis casts one more vote for the frictionless contact.

6 Conclusion

The ICL at MIT has successfully completed the second Sandia Fracture Challenge concerning an S-shaped challenge specimen made from a Ti–6Al–4V sheet with

two starter notches and three holes. A blind prediction of the crack path and the force–COD1 curve during the tensile test of the specimen at slow and fast loading speeds was made, using a Hill'48 yield function and a modified Johnson–Cook model incorporating a combined Swift–Voce strain hardening law. Treating temperature as an internal variable, its evolution was approximated without solving thermal field equations. The onset of fracture was predicted by a rate-dependent Hosford–Coulomb fracture initiation model. After the blind prediction, a leftover sheet was fully characterized with a comprehensive testing and modeling program. A significant improvement in the prediction was achieved. The key findings are summarized as follows.

1. In the framework of a non-associated flow rule, the Hill'48 anisotropic yield function is able to predict the plastic anisotropy of the Ti–6Al–4V sheet with great accuracy and computational efficiency. To obtain an even higher level of accuracy, especially for uniaxial tension in the diagonal direction and the smiley shear specimen, a more complex yield function and anisotropic hardening could be required.
2. An accurate description of the hardening curve at large strains is crucial for predicting ductile fracture. It is achieved by linearly combining the Swift and the Voce strain hardening laws. It is emphasized that the calibration should be based on notched tension rather than uniaxial tension (dog-bone) specimens. Furthermore, even when treating temperature as an internal variable instead of performing a fully-coupled thermo-mechanical analysis, the Johnson–Cook strain rate hardening and temperature softening functions are able to accurately model the dynamic flow stress of the Ti–6Al–4V sheet.
3. The strain rate dependent Hosford–Coulomb fracture initiation model can accurately predict the onset of fracture in the Ti–6Al–4V sheet at different strain rates. Besides the global crack path, B–D–E–A, and the COD1 at fracture, the applied plasticity and fracture modeling approach is able to correctly predict the first crack initiation in the D–E ligament.
4. The low yield stress under shear turns out to originate from anisotropy, so the effect of the Lode angle can be neglected in the plasticity standpoint. However, its influence on ductile fracture cannot

be ignored to ensure the accuracy of predicting the onset of fracture.

Acknowledgments The authors are grateful for the financial support from the MIT Industrial Fracture Consortium. Thanks are due to Professor Tomasz Wierzbicki (MIT) and Dr. Borja Erice (ETH Zurich) for valuable discussions. Sandia National Laboratories are thanked for providing the Ti–6Al–4V alloy sheet. A free academic license for HyperMesh by Altair Engineering is also gratefully acknowledged.

References

- Abaqus (2016) Reference manuals v6.14-3. Abaqus Inc
- Bai Y, Wierzbicki T (2008) A new model of metal plasticity and fracture with pressure and Lode dependence. *Int J Plast* 24(6):1071–1096
- Bai Y, Wierzbicki T (2010) Application of extended Mohr–Coulomb criterion to ductile fracture. *Int J Fract* 161(1):1–20
- Bao Y, Wierzbicki T (2004) On fracture locus in the equivalent strain and stress triaxiality space. *Int J Mech Sci* 46(1): 81–98
- Barlal F, Brem JC, Yoon JW, Chung K, Dick RE, Choi SH, Pourboghrat F, Chu E, Lege DJ (2003) Plane stress yield function for aluminum alloy sheets. *Int J Plast* 19(9):1297–1319
- Boyce BL et al (2014) The Sandia Fracture Challenge: blind round robin predictions of ductile tearing. *Int J Fract* 186:5–68
- Boyce BL et al (2016) The second Sandia Fracture Challenge: prediction of ductile failure under quasi-static and moderate-rate dynamic loading. *Int J Fract* doi:10.1007/s10704-016-0089-7
- Cerrone A, Hochhalter J, Heber G, Ingrassia A (2014) On the effects of modeling as-manufactured geometry: toward digital twin. *Int J Aereosp Eng*. doi:10.1155/2014/439278
- Clausen AH, Børvik T, Hopperstad OS, Benallal A (2004) Flow and fracture characteristics of aluminium alloy AA5083-H116 as function of strain rate, temperature and triaxiality. *Mater Sci Eng A* 364(2):260–272
- Dunand M, Mohr D (2010) Hybrid experimental–numerical analysis of basic ductile fracture experiments for sheet metals. *Int J Solids Struct* 47(9):1130–1143
- Dunand M, Mohr D (2014) Effect of Lode parameter on plastic flow localization after proportional loading at low stress triaxialities. *J Mech Phys Solids* 66(133):153
- Erice B, Gálvez F, Cendón DA, Sánchez-Gálvez V (2012) Flow and fracture behaviour of FV535 steel at different triaxialities, strain rates and temperatures. *Eng Fract Mech* 79:1–17
- Gross AJ, Ravi-Chandar K (2014) Prediction of ductile failure using a local strain-to-failure criterion. *Int J Fract* 186:66–91
- Gross AJ, Ravi-Chandar K (2016) Prediction of ductile failure in Ti–6Al–4V using a local strain-to-failure criterion. *Int J Fract* doi:10.1007/s10704-016-0076-z
- Gurson AL (1977) Continuum theory of ductile rupture by void nucleation and growth: part I—yield criteria and flow rules for porous ductile media. *J Eng Mater Technol* 99(1):2–15

- Hill R (1948) A theory of the yielding and plastic flow of anisotropic metals. *Proc R Soc Lond Ser A* 193:281–297
- Hosford WF (1972) A generalized isotropic yield criterion. *J Appl Mech* 39(2):607–609
- Huh J, Huh H, Lee CS (2013) Effect of strain rate on plastic anisotropy of advanced high strength steel sheets. *Int J Plast* 44:23–46
- Johnson GR, Cook WH (1983) A constitutive model and data for metals subjected to large strains, high strain rates and high temperatures. In: 7th international symposium on ballistics, The Hague, pp 541–547
- Khan AS, Huang S (1992) Experimental and theoretical study of mechanical behavior of 1100 aluminum in the strain rate range 105 to 104s⁻¹. *Int J Plast* 8:397–424
- Kocks UF, Argon AS, Ashby MF (1975) *Thermodynamics and kinetics of slip*. Pergamon Press, Oxford, New York
- Lemaitre J (1985) A continuous damage mechanics model for ductile fracture. *J Eng Mater Technol* 107(1):83–89
- Li Y, Wierzbicki T, Sutton MA, Yan J, Deng X (2010) Mixed mode stable tearing of thin sheet Al 6061–T6 specimens: experimental measurements and finite element simulations using a modified Mohr–Coulomb fracture criterion. *Int J Fract* 210(14):1858–1869
- Lou Y, Huh H, Lim S, Pack K (2012) New ductile fracture criterion for prediction of fracture forming limit diagrams of sheet metals. *Int J Solids Struct* 49(25):3605–3615
- Marcadet SJ, Mohr D (2015) Effect of compression–tension loading reversal on the strain to fracture of dual phase steel sheets. *Int J Plast* 72:21–43
- McClintock F (1968) A criterion of ductile fracture by the growth of holes. *J Appl Mech* 35(2):9
- Mohr D, Dunand M, Kim KH (2010) Evaluation of associated and non-associated quadratic plasticity models for advanced high strength steel sheets under multi-axial loading. *Int J Plast* 26(7):939–956
- Mohr D, Marcadet S (2015) Micromechanically-motivated phenomenological Hosford–Coulomb model for predicting ductile fracture initiation at low stress triaxialities. *Int J Solids Struct* 67–68:40–55
- Nahshon K, Hutchinson JW (2008) Modification of the Gurson model for shear failure. *Eur J Mech A Solids* 27(1):1–17
- Nahshon K, Miraglia M, Cruce J, DeFrese R, Moyer ET (2014) Prediction of the Sandia Fracture Challenge using a shear modified porous plasticity model. *Int J Fract* 186:93–105
- Neilsen M, Dion K, Fang HE, Kaczmarowski AK, Karasz E (2014) Ductile tearing predictions with Wellman’s failure model. *Int J Fract* 186:107–114
- Nielsen KL, Tvergaard V (2010) Ductile shear failure or plug failure of spot welds modelled by modified Gurson model. *Eng Fract Mech* 77(7):1031–1047
- Pack K, Luo M, Wierzbicki T (2014) Sandia Fracture Challenge: blind prediction and full calibration to enhance fracture predictability. *Int J Fract* 186:155–175
- Pack K, Marcadet SJ (2016) Numerical failure analysis of three-point bending on martensitic hat assembly using advanced plasticity and fracture models for complex loading. *Int J Solids Struct*. doi:10.1016/j.ijsolstr.2016.02.014
- Rice JR, Tracey DM (1969) On the ductile enlargement of voids in triaxial stress fields. *J Mech Phys Solids* 17(3):201–217
- Roth CC, Mohr D (2014) Effect of strain rate on ductile fracture initiation in advanced high strength steel sheets: experiments and modeling. *Int J Plast* 56:19–44
- Roth CC, Mohr D (2016) Ductile fracture experiments with locally proportional loading histories. *Int J Plast* doi:10.1016/j.ijplas.2015.08.004
- Rusinek A, Klepaczko JR (2001) Shear testing of a sheet steel at wide range of strain rates and a constitutive relation with strain rate and temperature dependence of the flow stress original research article. *Int J Plast* 17(1):87–115
- Smerd R, Winkler S, Salisbury C, Worswick M, Lloyd D, Finn M (2005) High strain rate tensile testing of automotive aluminum alloy sheet. *Int J Impact Eng* 32:541–560
- Stoughton TB (2002) A non-associated flow rule for sheet metal forming. *Int J Plast* 18:687–714
- Stoughton TB, Yoon JW (2009) Anisotropic hardening and non-associated flow in proportional loading of sheet metals. *Int J Plast* 9:1777–1817
- Swift HW (1952) Plastic instability under plane stress. *J Mech Phys Solids* 1:1–18
- Tancogne-Dejean T, Roth CC, Woy U, Mohr D (2016) Probabilistic fracture of Ti-6Al-4V made through additive layer manufacturing. *Int J Plast* 78:145–172
- Tvergaard V, Needleman A (1984) Analysis of the cup-cone fracture in a round tensile bar. *Acta Metall* 32(1):157–169
- Verleysen P, Peirs J, van Slycken J, Faes K, Duchene L (2011) Effect of strain rate on the forming behaviour of sheet metals. *J Mater Process Technol* 211(8):1457–1464
- Voce E (1948) The relationship between stress and strain for homogeneous deformation. *J Inst Metals* 74: 537–562
- Voyiadjis GZ, Abed FH (2005) Microstructural based models for bcc and fcc metals with temperature and strain rate dependency. *Mech Mater* 37:355–378
- Wang K, Luo M, Wierzbicki T (2014) Experiments and modeling of edge fracture for an AHSS sheet. *Int J Fract* 187(2):245–268
- Xue L (2007) Damage accumulation and fracture initiation in uncracked ductile solids subject to triaxial loading. *Int J Solids Struct* 44:5163–5181
- Xue L (2008) Constitutive modeling of void shearing effect in ductile fracture of porous materials. *Eng Fract Mech* 75(11):3343–3366
- Zhang T, Fang E, Liu P, Lua J (2014) Modeling and simulation of 2012 Sandia fracture challenge problem: phantom paired shell for Abaqus and plane strain core approach. *Int J Fract* 186:117–139
- Zerilli FJ, Armstrong RW (1987) Dislocation-mechanics-based constitutive relations for materials dynamics calculations. *J Appl Phys* 61:1816–1825